AGU100 ADVANCING EARTH AND SPACE SCIENCE

JGR Solid Earth

RESEARCH ARTICLE
10.1029/2019JB018229

Water Availability and Deformation Processes in Smectite-Rich Gouges During Seismic Slip

S. Aretusini[1], E. Spagnuolo[1], M. C. Dalconi[2], G. Di Toro[1,2], and E. H. Rutter[3]

[1]Sezione di Tettonofisica e Sismologia, Istituto Nazionale di Geofisica e Vulcanologia, Roma, Italy, [2]Dipartimento di Geoscienze, Università degli Studi di Padova, Padova, Italy, [3]School of Earth and Environmental Sciences, University of Manchester, Manchester, UK

Key Points:
- In smectite-rich gouges, deformation processes associated with seismic slip depend on the availability of water and slip velocity
- Under partly saturated conditions, water mechanical pressurization and thermal pressurization (>0.01 m/s) control shear strength
- Under dry conditions, cataclasis (0.001–0.1 m/s) and grain size sensitive flow or frictional melting (1.3 m/s) control shear strength

Supporting Information:
- Supporting Information S1

Correspondence to:
S. Aretusini,
stefano.aretusini@ingv.it

Citation:
Aretusini, S., Spagnuolo, E., Dalconi, M. C., Di Toro, G., & Rutter, E. H. (2019). Water availability and deformation processes in smectite-rich gouges during seismic slip. *Journal of Geophysical Research: Solid Earth*, *124*, 10,855–10,876. https://doi.org/10.1029/2019JB018229

Received 18 JUN 2019
Accepted 17 SEP 2019
Accepted article online 14 OCT 2019
Published online 6 NOV 2019

Abstract Smectite clays occur in subduction zone fault cores at shallow depth (approximately 1 km; e.g., Japan Trench) and landslide décollements (e.g., Vajont, Italy, 1963). The availability of pore fluids affects the likelihood that seismic slip propagates from deeper to shallow fault depths or that a landslide accelerates to its final collapse. To investigate the deformation processes active during seismic faulting we performed friction experiments with a rotary machine on 2-mm-thick smectite-rich gouge layers (70/30 wt % Ca-montmorillonite/opal) sheared at 5-MPa normal stress, at slip rates of 0.001, 0.01, 0.1, and 1.3 m/s, and total displacement of 3 m. Experiments were performed on predried gouges under vacuum, under room humidity and under partly saturated conditions. The fault shear strength measured in the experiments was included in a one-dimensional numerical model incorporating frictional heating, thermal, and thermochemical pressurization. Quantitative X-ray powder diffraction and scanning electron microscopy investigations were performed on pristine and deformed smectite-rich gouges. Under dry conditions, cataclasis and amorphization dominated at slip rates of 0.001–0.1 m/s, whereas grain size sensitive flow and, under vacuum, frictional melting occurred at fast slip rates (1.3 m/s). Under partly saturated conditions, frictional slip in a smectite foliation occurred in combination with pressurization of water by shear-enhanced compaction and, for V = 0.01–1.3 m/s, with thermal pressurization. Pseudotachylytes, the only reliable microstructural markers for seismic slip, formed only with large frictional power (>2 MW/m^2), which could be achieved at shallow depth with high slip rates, or, at depth, with high shear stress in dehydrated smectites.

1. Introduction

Smectite clay minerals are 2:1 layer silicates whose structure is constituted by two tetrahedral sheets and one octahedral sheet. Between two consecutive 2:1 layers, in the basal planes (i.e., the interlayers), partially charged cations bonded to water molecules control the frictional strength of this mineral (Behnsen & Faulkner, 2013; Moore & Lockner, 2007; Sánchez-Roa et al., 2017). Smectite clay minerals were found in slipping zones located in landslide décollements (Hendron & Patton, 1987) and in the fault cores of plate-boundary mature faults (Mg-saponite, Holdsworth et al., 2011) and subduction zone faults (montmorillonite in Barbados and Japan Trench; Vrolijk, 1990). They also occur as minor constituents in seismogenic faults at shallow depth (<5 km; Carpenter et al., 2011; Kuo et al., 2009; Rutter et al., 1986; Sone et al., 2012; Tesei et al., 2015; Vrolijk, 1990; Wu et al., 1975). This is because smectite is a common alteration mineral of silicates (e.g., feldspars) and a devitrification product of glassy rocks (e.g., basalts, tephra). In natural faults, the stability field of smectite minerals controls on-fault frictional strength, stability of friction, and seismogenic slip propagation in the shallow crust. The upper bound of the smectite stability field can be set at 150 °C, where the smectite interlayers are fully and irreversibly dehydrated (Schleicher et al., 2015) and the transformations to interstratified smectite/illite and then illite occur (Vrolijk, 1990), depending on the availability (i.e., chemical activity) of potassium ions. Depending on the tectonic setting and geothermal gradient, the depth corresponding to this temperature can vary between 5 km in continental areas (average geothermal gradient of 30 °C/km), increasing to 15 km in subduction zones (average geothermal gradient of 10 °C/km; Kearey et al., 2013). In general, only at crustal depths of less than 10 km can smectite clay minerals influence the mechanical behavior of faults. On the other hand, smectite is stable at near-surface conditions and therefore may control the mechanical behaviour of landslides (Nakamura et al., 2010).

Rock deformation experimental studies broadly have shown how the degree of water saturation (or water content) strongly affects the strength and stability of friction of montmorillonite, a common smectite mineral, both at subseismic (Morrow et al., 2017, and references therein) and seismic slip rates (Bullock et al., 2015; Faulkner et al., 2011; Ujiie et al., 2011). Frictional properties of smectite-rich gouges under room humidity or vacuum-dry conditions have been studied with triaxial apparatuses (Behnsen & Faulkner, 2013; Morrow et al., 2017; Tembe et al., 2010) and under room humidity conditions in double direct-shear (Ikari et al., 2007; Saffer & Marone, 2003) and rotary shear machines (Aretusini et al., 2017; Bullock et al., 2015; Ferri et al., 2011; French et al., 2014; Han et al., 2014; Kitajima et al., 2010; Mizoguchi et al., 2007; Oohashi et al., 2015; Remitti et al., 2015). Although the gouges in these experiments were sheared for a range of amount of slip (i.e., from 1 mm to tens of meters), the dependence of friction on amount of slip has been poorly investigated (see discussion in Aretusini et al. (2017)). The main outcome for dry montmorillonite gouges is that the friction coefficient μ is velocity-dependent as follows: $\mu > 0.6$ for $V = 5$–300 μm/s (Ikari et al., 2007; Morrow et al., 2017), $\mu > 0.7$ for $V = 0.01$–0.1 m/s (Ferri et al., 2011), and $\mu < 0.3$ for $V = 1$–1.3 m/s (Bullock et al., 2015; Ferri et al., 2011; French et al., 2014; Remitti et al., 2015). The evolution with slip rate of the friction coefficient was concomitant, at subseismic slip rates, to wear and cataclasis associated with frictional slip on the smectite interlayers (Moore & Lockner, 2007) and, at seismic slip rates, to dehydration of smectite interlayers with the collapse to an illite-like structure (Ferri et al., 2011), frictional melting (Han et al., 2014), and thermal decomposition associated with vaporization of pore fluids (French et al., 2014; Ujiie et al., 2011).

During shearing of smectite aggregates under water-saturated conditions, because of their low permeability (approximately 10^{-23}–10^{-21} m^2; Behnsen & Faulkner, 2011, 2013), pore pressures remained constant only at subseismic slip rates (V of 0.05 μm/s) or when the characteristic time duration of the experiment was larger than the time required for fluids to flow through interconnected pores (Faulkner et al., 2018; Moore & Lockner, 2007; Morrow et al., 2017; Wojatschke et al., 2016). The main outcome of experiments performed under equilibrated pore pressure conditions is that the friction coefficient increases with normal stress from 0.1 at 5 MPa to 0.25 at 100 MPa, as a result of frictional strength increasing with decreasing thickness of the interlayer water films due to water extrusion with pressure (Moore & Lockner, 2007). Although the experiments performed at low slip rates allowed authors to ensure saturated conditions, these experiments did not reproduce seismic slip rates. Instead, experiments performed with rotary shear machines do reproduce seismic slip rates but not the achievement of equilibrated pore pressures and the pore fluid pressure is not generally measurable (Faulkner et al., 2011; Ujiie et al., 2013). Despite these limitations, experiments performed under "wet" but nonsaturated conditions, at seismic slip rates (from 0.001 to 1.3 m/s) and at low normal stresses (below 9 MPa), resulted in (i) very low friction coefficient at the initiation of sliding due to pore pressure buildup via thermal pressurization (Boutareaud et al., 2008; Brantut et al., 2008; Bullock et al., 2015; Faulkner et al., 2011; Ferri et al., 2011; French et al., 2014; Oohashi et al., 2015; Remitti et al., 2015; Sawai et al., 2014; Ujiie et al., 2011, 2013; Vannucchi et al., 2017); (ii) a minimum friction coefficient (often corresponding to the so-called "steady state" friction coefficient), decreasing with increasing slip rate from 0.15 to 0.2 at $V = 0.01$ m/s to 0.05 at 1.3 m/s (Ferri et al., 2011; French et al., 2014; Oohashi et al., 2015; Sawai et al., 2014); and (iii) negligible shear fracture energy dissipation (Bullock et al., 2015; Faulkner et al., 2011). Such a low dissipation of energy during the propagation of the seismic rupture would promote, under some given loading conditions, seismic rupture propagation up to the surface (Vannucchi et al., 2017). Under water-saturated conditions, the decrease of friction coefficient with slip at subseismic slip rates was observed in association with the development of a foliation composed of aligned smectite crystals and, at seismic slip rates, with the formation of foliated and fluidized microstructures. These features were interpreted to be the result of frictional slip on smectite basal planes (Aretusini et al., 2019) and also associated with vaporization of pore water (French et al., 2014; Ujiie et al., 2011).

Despite the relevance of deformation processes in smectite to earthquake mechanics, a systematic study is still lacking and the physical mechanisms explaining frictional evolution with slip remain largely debated. This study integrates rotary shear friction experiments performed under variable water content (from vacuum dry to partly saturated conditions), permeability measurements, microstructural analysis, analysis of amorphous content, and modeling of thermochemical and thermal pressurization to discuss the deformation processes in smectite-rich gouges and their relevance to natural earthquakes.

2. Materials and Methods

2.1. Starting Material and Sample Preparation

We performed all the experiments on source clay STx-1b (Clay Mineral Society), composed of 70 wt % Ca-montmorillonite and 30 wt % opal interstratified with cristobalite and tridymite (opal-CT; Chipera & Bish, 2001). To observe the influence of water content in smectite during deformation at seismic slip rates, three batches of synthetic clay gouges were prepared according to the following treatment scheme: (i) equilibrated with room humidity (20–45%) and temperature (25–28 °C), (ii) oven-dried at 100 °C for 12 hr; and (iii) oven-dried at 150 °C for 24 hr. Before the experiments, the pre-heated gouges were placed in a desiccator to cool down to room temperature and to avoid the gouges to adsorb water and equilibrate with room humidity conditions.

2.2. Permeability Measurements

Permeability measurements were performed on the room-equilibrated starting material using the pore pressure oscillation method (Bernabé et al., 2006; David et al., 2018; Turner, 1958). A 4-mm-thick dry gouge layer was sandwiched between two aluminum half-cylinders, cut parallel to the cylindrical axis. The sample was jacketed, first with a neoprene jacket and then with a heat-shrink rubber tube. The jacketed sample was loaded into a high-pressure permeameter (as described by McKernan et al. (2017)). The permeameter used synthetic oil (di-octyl sebacate) as the confining medium and argon as the pore pressure medium, so that permeability was measured under nominally dry conditions (cf. Behnsen & Faulkner, 2011).

The sample assembly was placed within the permeameter and then a confining pressure was applied (ranging up to 45 MPa). A baseline pore pressure (normally 15 MPa) was applied at both the upstream and downstream sides of the sample. The application of effective pressure caused a reduction in thickness of the gouge layer through compaction. The reduced thickness, measured after the test, was used to infer the cross-sectional area of the flow path. At each effective pressure, after the applied pore pressure equilibrated, the downstream side was isolated, and pore pressure was varied at the upstream side in the form of a sinusoidal pressure variation of amplitude 1 MPa and a period (60 to 200 s) chosen to produce a downstream attenuation by at least 20%. The downstream pore pressure sinewave was measured and had the same period, smaller amplitude, and a phase shift compared to the upstream sinewave. The amplitude ratio and phase shift of downstream and upstream sinewaves were obtained by a best fit procedure and used to solve the general equation for dimensionless pore storage and permeability (Bernabé et al., 2006) using the gradient descent method. The dimensionless permeability was used to calculate permeability of the gouge layer, taking into account the temperature-dependent viscosity and pressure-dependent compressibility of the argon gas (Gosman et al., 1969; Michels et al., 1954; Younglove & Hanley, 1986), the period of the oscillating pore pressure, and length and thickness of the gouge layer (Text S1).

The permeability of the gouge layer was investigated under increasing steps of effective pressures (from 5 to 30 MPa) and under decreasing steps of effective pressure down to 5 MPa after the maximum effective normal stress was applied. In this way, the permeability was measured both at normally consolidated and overconsolidated states at every effective stress applied (Figure S1 and Table S1).

2.3. Low- to High-Velocity Friction Experiments

All the experiments conducted at seismic slip rates were performed with SHIVA (Slow to High Velocity Apparatus), installed at the HP-HT laboratory of INGV (Di Toro et al., 2010; Niemeijer et al., 2011; see Figure 1a). The sample assemblage used in the experiments discussed here is illustrated in Figure 1b. A pair of hollow stainless-steel specimen holders (15/25-mm inner/outer radii) were combined with two Teflon parts: a cylinder inserted in the inner hole and a ring positioned externally. The outer ring was cut at approximately 60° to its basal surface, tightened to the metal gouge holders with a stainless-steel hose clamp and fixed with screws to the rotational hollow cylinder. This dampened spurious oscillations and reduced extrusion of the gouge from the sample holder, improving the quality of the mechanical data. The gouge was weighed, so that nominally 3.2 g was placed in the sample holder.

Eight experiments were performed on the room-equilibrated gouge: four under room humidity conditions, with average 50% relative humidity (previously published in Aretusini et al. (2017)), and four under partly saturated conditions by adding 0.5 mL of de-ionized water to the gouge layer (previously published in

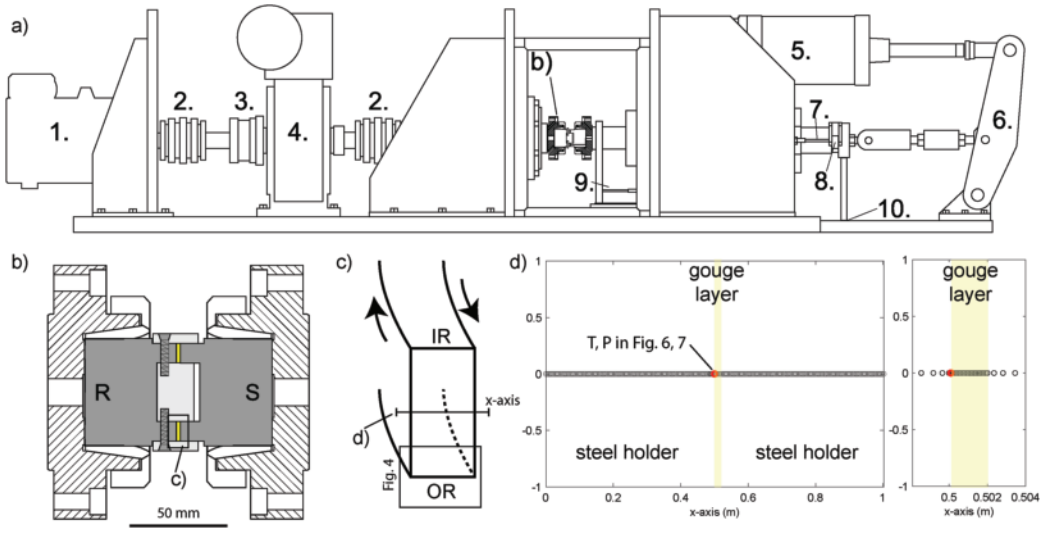

Figure 1. Sketch of SHIVA rotary shear apparatus, sample holder, and thermal model with mesh. (a) Sketch of SHIVA rotary shear apparatus: "big" electric motor (1), transmission (2), free-wheel clutch (3), "small" electric motor and gear box (4), air actuator (5), force multiplier lever (6), DC-LVDT (7), axial force load cell (8), LVDT (9), position of torque load cell (10) (section 2.3). (b) Sample holder used for rotary shear experiments: the gouge layer (yellow) is sandwiched between two stainless steel sample holders (dark grey) and confined laterally by Teflon rings (light grey) anchored to the sample holder on the rotary side. "R" and "S" indicate rotary and stationary side, respectively. (c) The orientation of the SEM-BSE images with respective to the shear direction during the experiments: stationary side (S), rotary side (R), outer radius (OR), and internal radius (IR; Figure 4). (d) Transect across the gouge layer showing the model domains and mesh (section 4.1). The red circle is the model node at which plots in Figures 6 and 7 are referred to.

Aretusini et al. (2019)). An additional eight experiments were run on the preheated gouges under evacuated conditions (pressure in the experimental chamber below 5×10^{-4} mbar).

Given the sample holder size, rotational displacement and tangential velocity were referred to the radius $r = 20.2$ mm (i.e., the equivalent radius), and henceforth defined as the equivalent displacement and velocity (cf. Di Toro et al., 2010). The rotary shear experimental procedure involved applying a normal stress of 5 MPa and then imposing a trapezoidal velocity function with identical acceleration and deceleration of 6.4 m/s^2 to the target equivalent velocity of 0.001, 0.01, 0.1, and 1.3 m/s, and total displacement of 3 m (Table 1). During the experiments the mechanical data were acquired at 12,500 S/s and then downsampled to 125 or 1,250 S/s in the longer experiments, at lower slip rates. The shear stress, total normal stress, displacement, and equivalent velocity were determined using the method described in Shimamoto and Tsutsumi (1994) or Di Toro et al. (2010). The ratio of the shear to the total normal stress is the apparent friction coefficient and will be used to discuss the mechanical data. Because pore pressure was neither monitored nor controlled in experiments performed under partly saturated conditions, the effective normal stress could not be precisely resolved, and therefore, we could not calculate the friction coefficient, defined as the ratio between the shear strength and the effective normal stress. Axial displacement of the piston (arising from shortening and dilatancy of the gouge layer) was measured with a high-resolution linear variable displacement transducer (LVDT; resolution 100 nm; range 1 mm) installed next to the sample chamber (position 9 in Figure 1a) and a lower resolution LVDT (resolution 1 μm; range 50 mm) installed at the further end of the axial piston (position 7 in Figure 1a).

Using the shear stress τ and total slip D of the experiments, the total frictional work density, or the total work dissipated per unit surface area of the fault, was $\int_0^D \tau(x)\, dx$, (i.e., τ integrated over the entire fault slip D). The average frictional power density, or the average power dissipated per unit surface area of the fault, was obtained by dividing the frictional work density by the duration of the experiment.

The thickness of the gouge layer was determined with the high- and low-resolution axial displacement measurements, by subtracting the axial position without the gouge layer from the total axial displacement.

Table 1
The High-Velocity Friction Experiments Presented Here

Experiment no.	V (m/s)	d (m)	μ_p (-)	μ_{fin} (-)	FWD (MJ/m^2)	Δt (s)	FPD (MW/m^2)
Preheated at 150 °C, vacuum dry experiments							
s1533	0.001	3	0.77	0.93	11.05	2973.0	3.72E − 03
s1532	0.01	3	0.68	0.87	10.81	300.1	3.60E − 02
s1531	0.1	3	0.73	0.74	10.22	30.0	3.40E − 01
s1530	1.3	3	0.75	0.35	5.622	2.5	2.24E+00
Preheated at 100 °C, vacuum dry experiments							
s1479	0.001	3	0.85	0.92	9.76	2973.0	3.28E − 03
s1344	0.01	3	0.7	0.87	10.60	300.1	3.53E − 02
s1343	0.1	3	0.76	0.74	9.43	30.0	3.14E − 01
s1365	1.3	3	0.76	0.35	5.07	2.5	2.02E+00
Room-equilibrated, room humidity experiments							
s1472	0.001	3	0.52	0.85	8.56	2973.0	2.88E − 03
s1172	0.01	3	0.62	0.76	9.63	300.1	3.21E − 02
s1169	0.1	3	0.62	0.63	8.34	30.0	2.78E − 01
s1166	1.3	3	0.82	0.33	3.93	2.5	1.57E+00
Room-equilibrated, partly saturated experiments							
s1331	0.001	3	0.38	0.51	5.05	2973.0	1.70E − 03
(s1336)	0.001	3	0.38	0.52	5.46	2974.0	1.83E − 03
s1253	0.01	3	0.32	0.47	5.16	300.1	1.72E − 02
s1252	0.1	3	0.32	0.37	3.15	30.0	1.05E − 01
s1251c	1.3	3	0.34	0.08	0.37	2.5	1.47E − 01

Note. Experiment number (*exp*), slip rate (V; m/s), total displacement (d; m), peak and final friction coefficient (μ_p and μ_{fin}), frictional work density (FWD; MJ/m^2), duration of the experiment (Δt; s), and average frictional power density (FPD; MW/m^2).

The thickness of the gouge layer, measured at 5 MPa before the onset of slip, allowed calculation of the total volume of the gouge layer (V_{tot}) and therefore the initial porosity. The porosity was estimated as

$$\varphi = \frac{V_{tot} - V_s}{V_{tot}} \quad (1)$$

where V_{tot} is the total volume calculated from the starting gouge thickness w_0 and the inner and outer radii r_i and r_o as $V_{tot} = w_0 \cdot \pi\ (r_o^2 - r_i^2)$. The volume of solids, V_s, was calculated by dividing the mass of the gouge (3.2 g) by the average density of the minerals (2.35 g/cm^3).

2.4. X-ray Powder Diffraction Quantitative Phase Analysis and Estimation of the Mass of Amorphous Materials

Five X-ray powder diffraction (XRPD) measurements were performed on smectite-rich gouges recovered from the partly saturated experiments: four on the gouge layers recovered after the mechanical testing and one on the partly saturated starting material compacted at a normal stress of 5 MPa. Data were collected with a θ/θ diffractometer (PANalytical X'Pert Pro, University of Padova, Padova, Italy) equipped with a real time multiple strip detector (X'Celerator), using CoKα radiation (40 kV and 40 mA). The analytical technique was the same as used to determine the proportions of both mineral phases and amorphous material abundances within the smectite-rich gouges sheared under room-humidity conditions (Aretusini et al., 2017).

Prior to the XRPD analysis, the gouges were air dried and the entire layer thickness recovered to avoid partial sampling. The gouge layer was gently disaggregated with a pestle and mortar and 10 wt % of alumina (NIST SRM 676a) internal standard was added. The resulting powders were mounted on a zero background Si single crystal sample holder (diameter 16 mm). Diffraction data were acquired in the 3–85 °2θ range. The incident beam pathway included (in order) 1/4° divergence slit, Bragg Brentano^{HD} monochromator, 0.04 rad soller slits, and 1/2° antiscattering slit. The pathway of the diffracted beam included (in order) 5-mm antiscatter slit and 0.04 rad soller slits. Humidity in the measuring chamber was monitored and in the range 29–33% of relative humidity. Each sample was measured twice for data reproducibility.

Determination of both mineral phases and amorphous material weight fractions was performed using the combined Rietveld and reference intensity ratio methods (Gualtieri, 2000; Westphal et al., 2009). Rietveld

data analysis was performed using the Profex-BGMN software (Bergmann et al., 1998; Doebelin & Kleeberg, 2015). The instrumental assemblage and optics were simulated within BGMN using a Monte Carlo simulation. Structural models of the minerals recognized in the gouge were taken from the BGMN library for quartz, plagioclase, and alumina internal standard (NIST 676a). For Ca-montmorillonite, we used the structural model comprising the turbostratic disorder (Ufer et al., 2009), and for opal-CT we used a supercell model simulating the irregular cristobalite-tridymite interlayering (Kleeberg, p.c.). The Ca-montmorillonite (001) peak intensity is sensitive to preferred orientation during sample preparation, and peak position is extremely sensitive to the relative humidity in the measuring chamber. Refinement was therefore limited to the 12–60 °2θ range to exclude the (001) peak of Ca-montmorillonite.

2.5. Microstructural Analysis

After mechanical testing the gouge layers were dried in a desiccator (for at least 12 hr) and then embedded within epoxy resin (Epofix). Sectioning of samples was performed using diethylene glycol (i.e., water was not used) as lubricant, to inhibit disaggregation and swelling of the smectite-rich samples. Orientation of cut was perpendicular to the slip surface and parallel to sample radius (radial section; Figure 1c). Samples were polished using oil-based diamond suspensions on silk disks, down to 1/4-μm particle size. Twenty-two polished blocks were investigated with a FEI Quanta field emission scanning electron microscope (University of Manchester). Each radial section was investigated using back scattered electrons (BSE) images.

3. Results

3.1. Permeability and Porosity of the Starting Material

Permeability of starting material at an effective normal stresses of 5 MPa, the same as the applied normal stress during the rotary shear experiments, was $K = 1.3 \times 10^{-16}$ m^2. Permeability decreased to 3.9×10^{-19} m^2 at an effective normal stress of 30 MPa (Table S1). The initial porosity was in the 40–43% range in the vacuum dry and room humidity experiments and was 35% in partly saturated experiments. In the latter, the volume of pores (i.e., $V_p = V_{tot} - V_s$) was of 0.75–0.8 mL, higher than the volume of added water (0.5 mL). The degree of saturation was estimated to be 62–67%, confirming that the gouge layer was under partly saturated conditions before the beginning of frictional sliding.

3.2. Friction and Gouge Thickness Evolution With Slip

In the rotary shear experiments (Figures 2a–2d), μ evolved with displacement as follows. At the beginning of the experiment when the sample was accelerated to the assigned target velocity (e.g., $V = 0.1$ m/s), μ increased linearly, because of the elastic loading of the machine and of the gouge layer, and then nonlinearly, accommodating the initial deformation of the gouge layer, up to a maximum friction coefficient named "peak friction" or μ_p (stage 0). Stage 0 and μ_p were followed by stages 1 and 2 which evolved with slip depending on the imposed slip rate and environmental conditions as discussed below (see also insets in Figure 2).

Vacuum-dry conditions with gouges preheated at 150 °C. At slip rates between 0.001 and 0.1 m/s, μ_p was 0.7–0.85 and was followed by a very short duration slip weakening stage 1 (up to $d = 0.009$ m), and a long-duration slip strengthening or slip neutral stage 2 up to a μ_{fin} which decreased with increasing slip rate from 0.92 to 0.74. On the other hand, for $V = 1.3$ m/s, μ_p was 0.75 and stage 1 displayed slip weakening to a minimum $\mu_{fin} = 0.35$, increasing to $\mu_{fin,h} = 0.5$ at the end of the experiment (Figures 2a–2d).

Vacuum dry conditions with gouges preheated at 100 °C. At slip rates between 0.001 and 0.1 m/s, μ_p was 0.7–0.85 and was followed by a short-duration slip weakening stage 1 (approximately 0.003–0.01 m), a long-duration slip strengthening or slip neutral stage 2 up to a μ_{fin} which decreased with increasing slip rate from 0.92 to 0.74. On the other hand, for $V = 1.3$ m/s, μ_p was 0.76 and stage 1 displayed slip weakening to a minimum $\mu_{fin} = 0.35$ at the end of the experiment.

Room humidity conditions (Aretusini et al., 2017). At slip rates V between 0.001 and 0.1 m/s, μ_p increased with slip rate (from 0.5 to 0.64) and was followed by a slip weakening stage 1 (up to $d = 0.4$ m) and a slip strengthening stage 2 until the end of the experiment. The onset of stage 2 occurred at the same displacement $d = 0.4$ m at these slip rates ($V = 0.001$–0.1 m/s), but the amount of slip strengthening in stage 2 decreased with slip rate: μ_{fin} was 0.85, 0.76, and 0.63 for 0.001, 0.01, and 0.1 m/s, respectively. At $V = 1.3$ m/s, after $\mu_p = 0.82$,

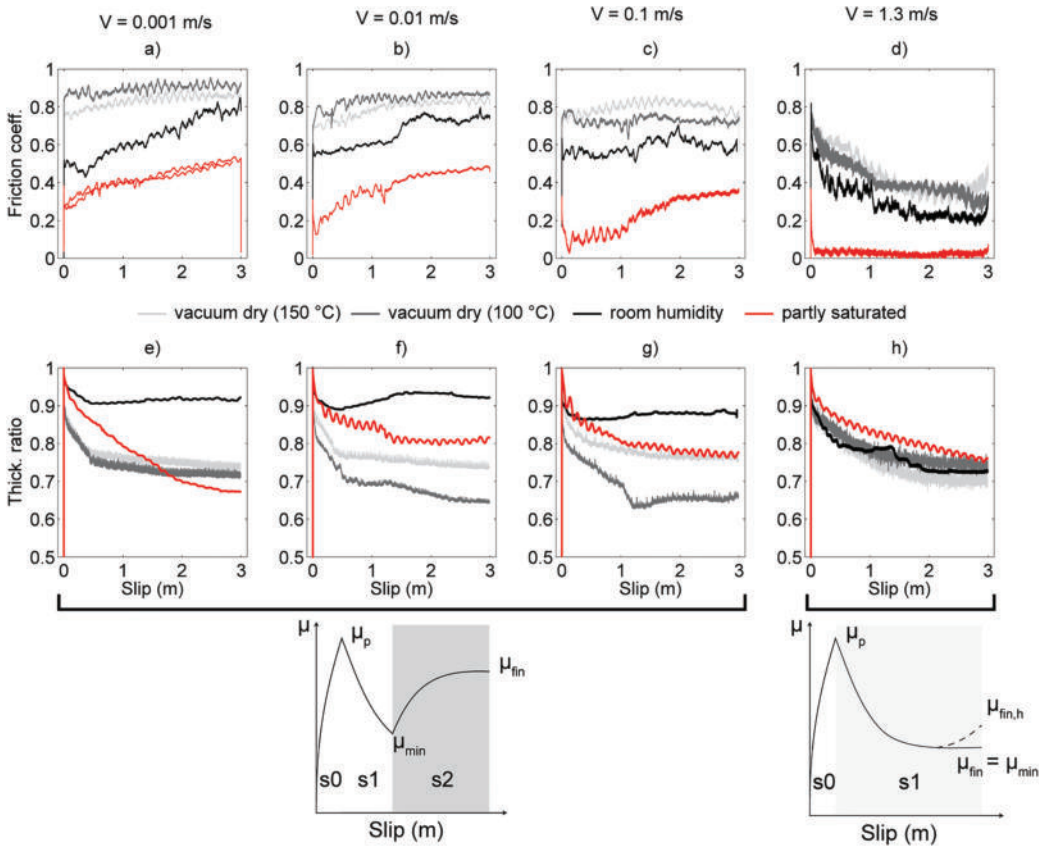

Figure 2. The rotary shear experiments. Each column represents all the starting materials deformed at the same slip rate of 0.001, 0.01, 0.1, and 1.3 m/s, respectively. Room humidity experiments are from Aretusini et al. (2017), and partly saturated experiments are from Aretusini et al. (2019). (a–d) Friction coefficient evolution with displacement. (e–h) Normalized thickness evolution with displacement.

stage 1 displayed slip weakening to a minimum $\mu_{fin} = 0.2$, increasing to $\mu_{fin,h} = 0.3$ at the end of the experiment. In summary, all the preheated materials sheared under vacuum dry and room humidity conditions displayed, once μ_p was achieved, slip hardening or slip neutral behavior for $V = 0.001$–0.1 m/s and slip-weakening for $V = 1.3$ m/s.

Water partly saturated conditions (Aretusini et al., 2019). Peak friction μ_p was very reproducible at all slip rates (0.31–0.38) and about 50% of the μ_p sheared under vacuum dry and room humidity conditions. At $V = 0.001$–0.1 m/s, in stage 1, the gouge showed slip weakening up to $d = 0.12$ m, and then slip strengthening (stage 2) until the end of the experiment. The onset of stage 2 occurred at progressively higher displacements with increasing slip rates and the amount of strengthening in stage 2 decreased with increasing slip rate (μ_{fin} was 0.51, 0.47, and 0.37 at 0.001, 0.01, and 0.1 m/s, respectively) until vanishing at $V = 1.3$ m/s. At $V = 1.3$ m/s, after an initial $\mu_p = 0.37$, stage 1 displayed slip weakening to a very low $\mu_{min} = 0.03$ after 0.08 m of slip. Then the friction coefficient remained constant and increased slightly to $\mu_{fin,h} = 0.08$ during velocity deceleration at the end of slip.

The gouge layer thickness was normalized to the initial thickness at the onset of slip to compare the thickness evolution of all the experimental data whilst avoiding the scatter due to the variation in initial thickness (e.g., a larger compaction was achieved in the partly saturated experiments before the onset of slip). Vacuum dry and partly water saturated experiments resulted in compaction, independently of the imposed slip rate, while room humidity experiments resulted in dilatation after approximately 1 m of slip at all slip rates, though dilatation was followed by further compaction for the experiment performed at 1.3 m/s (Figures 2e and 2f).

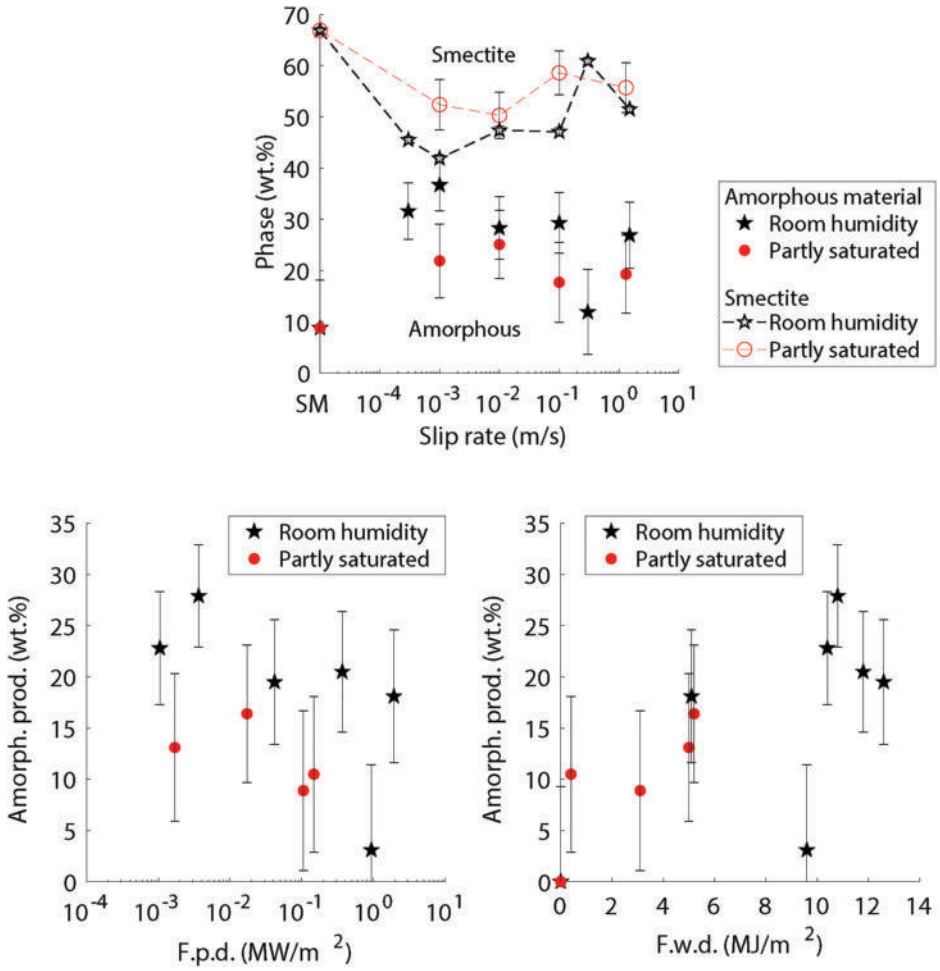

Figure 3. Amorphous material production in room humidity and (water) partly saturated experiments. Analysis of partly saturated experiments is compared with the analyses of room humidity experiments in Aretusini et al. (2017). (a) Amorphous (points) and smectite content (points and lines) versus the slip rate of the experiment. Composition of pristine gouges is labeled as "SM" (b) amorphous production with frictional power density *FPD* and (c) amorphous production with frictional work density *FWD*.

3.3. Mineralogical Composition and Amorphous Content

Mineralogical proportions and amorphous content obtained by quantitative XRPD analysis on the gouge layers are compared in Figure 3 and Table S2. Under both room humidity and partly saturated conditions, the amount of amorphous material produced during frictional sliding was inversely correlated to the smectite content (Ca-montmorillonite; Figure 3a) and the content of the other mineral phases did not change (Table S2). This suggested that amorphous material was derived from mechanical breakdown of the Ca-montmorillonite. The amorphous content was systematically higher in the gouges sheared under room humidity conditions compared to partly saturated conditions, at all slip rates. Among the room humidity and partly saturated experiments, amorphous content was higher at low slip rates and lower at high slip rates (Figure 3a).

The quantity of amorphous material produced was calculated as the difference between the amorphous material after the experiment and the amorphous material identified in the nonsheared starting material. The amorphous material production decreased with increasing frictional power density for both room humidity and partly saturated experiments (Figure 3b), which was analogous to the observed decrease of amorphous content with the slip rate of the experiment (compare with Figure 3a). The amorphous production increased with increasing frictional work density (Figure 3c). All partly saturated experiments

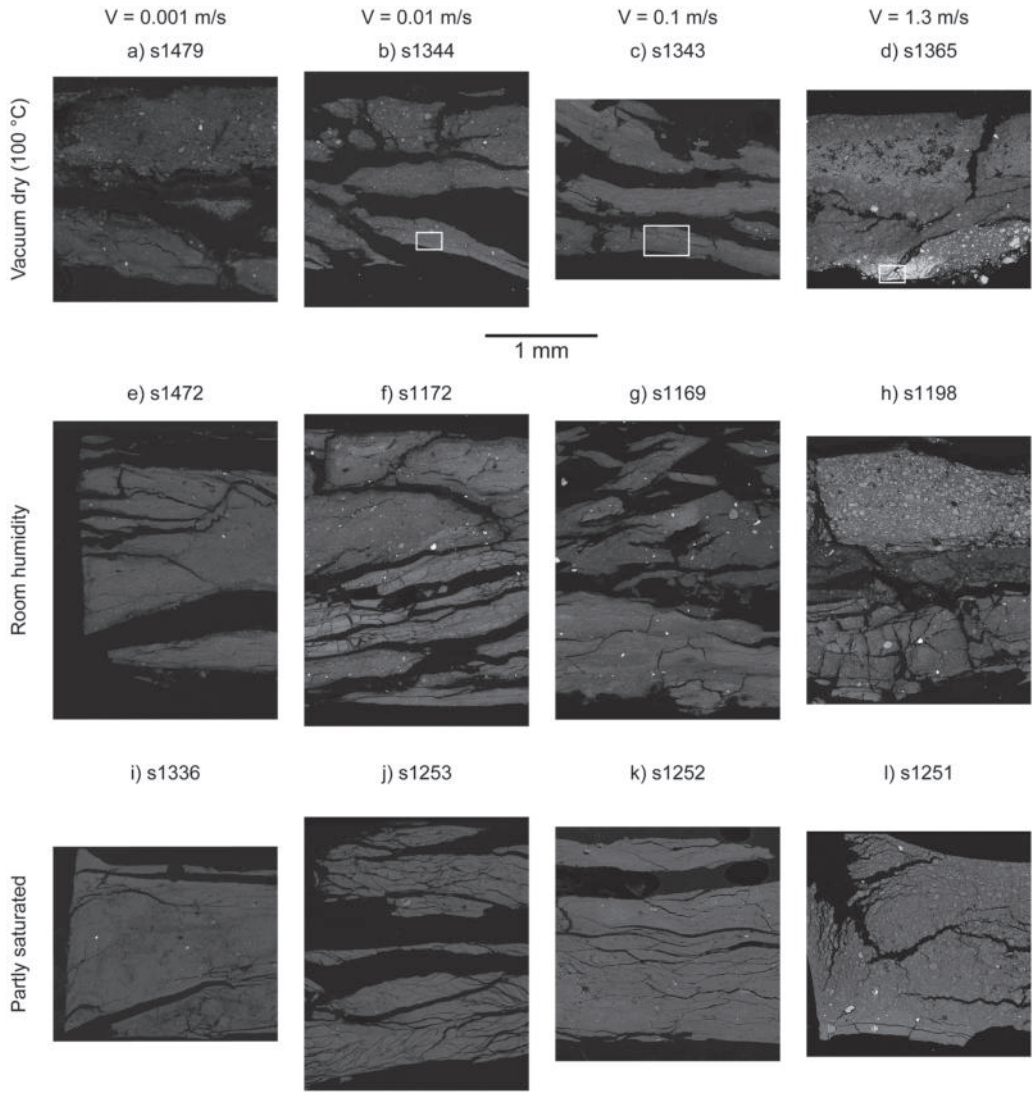

Figure 4. SEM-BSE images of the gouge layers, radial sections oriented as in Figure 1c, with stationary side at the bottom and outer radius on the left, orthogonal to the shear direction. The rows represent the types of starting materials and the columns represent the slip rates of the experiments (0.001, 0.01, 0.1, and 1.3 m/s, respectively).

had lower frictional work density (<6 MJ/m^2) compared to the room humidity ones, indicative of the positive correlation of amorphous material production with frictional work density (Aretusini et al., 2017).

3.4. Microstructures

Scanning electron microscope back-scattered electron (SEM-BSE) images of the gouge layers were acquired over the whole radial sections to recognize diagnostic features of the deformation processes activated during slip (Figures 4 and S2). In some cases, the interpretation of the microstructures suffered from the incomplete sampling of the gouge layers, as a result of fragmentation and dispersion in epoxy mounting resin and poor impregnation arising from the low permeability of the fine-grained matrix. The investigated samples were radial sections of the gouge layers (Figures 1c and 1d). Because of this orientation with respect to the sense of shear, kinematic indicators could not be observed. However, the orientation of the sections allowed us to appreciate the textural variations with slip and slip rate which developed along the radial position of the cut.

Vacuum dry and room humidity conditions. In the case of the experiments performed at V = 0.001–0.1 m/s, the gouge layer was sheared over the whole thickness and the microstructures formed in vacuum dry

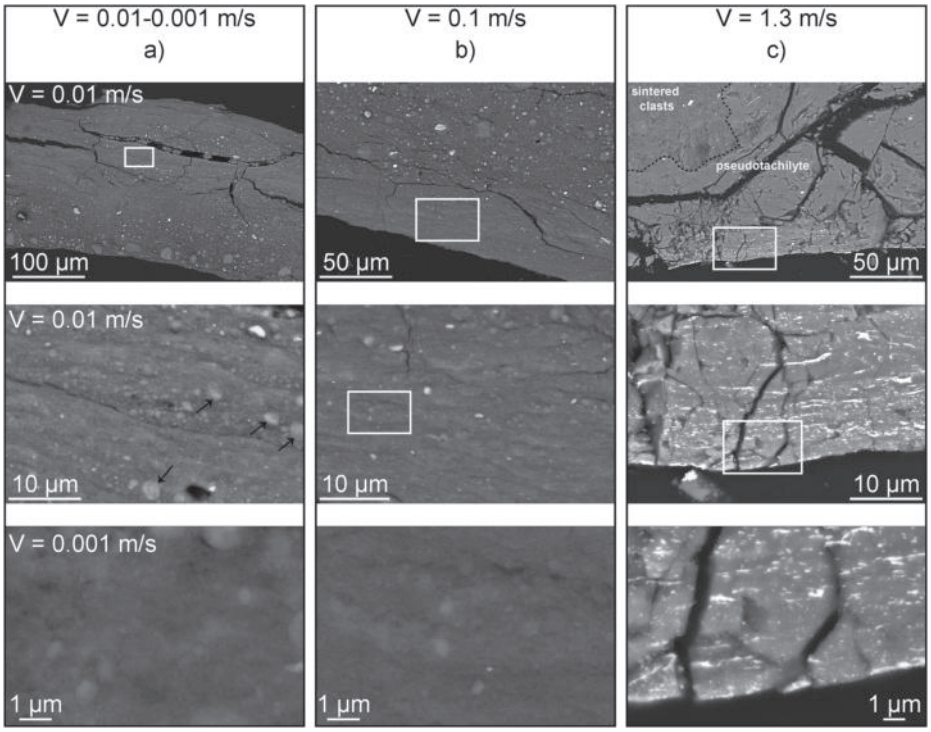

Figure 5. Detailed microstructures of vacuum dry experiments (SEM-BSE images). (a) Gouge layer deformed at 0.01 and 0.001 m/s (experiments s1344 and s1479) with increasing magnification. The gouge layer was organized in volumes with coarser clasts crosscut by bands of ultrafine clasts. In the latter, occasional CCAs are found (indicated by arrows). The bands contained submicrometric clasts, possibly nanoparticles. (b) Gouge layer deformed at 0.1 m/s (experiment s1343) with increasing magnification. The gouge layer was organized into volumes with coarser clasts crosscut by bands of ultrafine clasts. (c) Gouge layer deformed at 1.3 m/s (experiment s1365). The gouge layer at the stationary boundary contained a pseudotachylite ("PST") bordered with a volume of sintered clasts. Within the pseudotachylite the brighter spots were likely detached parts of the steel sample holder.

experiments appeared quite similar those produced in room humidity experiments (Figures 4a–4c and 4e–4g). The gouge layer was made of a matrix-rich microstructure containing clay cortex aggregates (cf. Boutareaud et al., 2008), indicated by arrows in Figure 5a, middle panel) cut by bands of ultrafine material (brighter under SEM-BSE; Figures 4a–4c and 4e–4g). These bands can be subplanar to wavy and they often act as cleavage surfaces for splitting of the gouge layer (Figures 5a and 5b, top panels). In the room humidity experiments, previous TEM investigations showed that the ultrafine bands were made of nanoparticles (<100 nm in size). In the vacuum dry experiments performed at V = 0.001–0.1 m/s, micrometric to submicrometric size clasts were found within these bands, comparable to the nanoparticles previously observed in room humidity experiments (Figures 5a and 5b, bottom panels).

In the case of the experiments performed at 1.3 m/s, at least half of the gouge layer preserved the same fabric of the starting material and strain was localized in the remaining thickness (Figures 4d, 4h, S2, and S3). However, unlike in the experiments performed at lower slip rates, the microstructure of the sheared gouges varied dramatically with ambient conditions. Under vacuum-dried conditions, strain was localized in a pseudotachylyte, as attested by the presence of a homogenous glassy-like matrix with a gradual transition to volumes of sintered clasts (Figures 4d and 5c). Instead, under room humidity conditions, pseudotachylytes were not found and strain was localized in a matrix-rich domain made of nanoparticles (<100 nm in size) wrapping CCAs (Figure 4h; for details, see Aretusini et al., 2017).

Partly saturated conditions. At all the investigated slip rates, the gouge layer contained a matrix-rich microstructure, which was foliated down to the nanoscale due to the preferential alignment of the long axis of the smectite grains (Aretusini et al., 2019). The gouge layer was split along the wavy nanofoliation (Figures 4i–4l). The main difference between the experiments performed at a slip rate of 1.3 m/s and those

performed at lower slip rates, was the thickness of the high-strain sheared domain: thin (< 0.1 mm) for the former, thick (the entire gouge layer) for the low slip rate experiments (Figure 4l).

4. Discussion

4.1. Thermochemical and Thermal Pressurization Model

Thermo-chemical pressurization was proposed to control the evolution of shear strength during seismic slip in smectite-rich gouges (Ferri et al., 2011). An overall increase in pore pressure and reduction in shear strength is expected due to water released by chemical reactions with temperature rise by frictional heating. Water can either be released from hydrated cation complexes in the smectite interlayers (dehydration), from opal during the opal-CT to quartz reaction, and from the octahedral sites of smectite (dehydroxylation). In addition, with temperature rise by frictional heating, pore pressure increases by thermal pressurization due to the higher thermal expansion of pore fluid compared to the thermal expansion of pore spaces (Rice, 2006; Wibberley & Shimamoto, 2005).

Previous studies proposed that dynamic weakening at seismic slip rates occurred by an increase of pore pressure, also in experiments performed under room humidity conditions (= no liquid water in the starting material). This was based on the following evidence: (i) gouge layer dilatancy during sliding inferred from the mechanical data (Ferri et al., 2010), (ii) presence of fluidal microstructures in the sheared gouges (Ferri et al., 2011; French et al., 2014; Ujiie et al., 2011) and the collapse of smectite to an illite-like structure during frictional sliding (Ferri et al., 2011), and (iii) direct measurement of pore fluid pressure during shearing (Chen, Niemeijer, Yao, et al., 2017). Since (i) the temperature evolution and increase during shearing and frictional heating and (ii) the pressure increase in the sheared gouge were very difficult to measure reliably, they were estimated with numerical models encompassing coupled thermo-hydro-mechano-chemical processes in clay-rich fault gouges (Chen et al., 2013). Additionally, the change in physical state of water from liquid to vapor was proposed to further promote pore fluid pressurization (Chen, Niemeijer, & Fokker, 2017; Ujiie et al., 2011).

In the partly saturated case, requiring neither a temperature increase by frictional heating nor seismic slip rates, the decrease of porosity with shear deformation was shown to induce a pore pressure increase (and a consequent transient decrease in frictional strength) depending on the permeability and thickness of the gouge layer (Faulkner et al., 2018: experiments were performed at subseismic slip rates). Given the very low permeability of the smectite-rich gouges, and the very short time duration (<3 s) of the experiments performed at seismic slip rates, pore fluid pressurization by inelastic reduction of pore volume is expected both statically during the normal stress increase and also dynamically during the experiments. However, because the gouge layer was not perfectly sealed and saturated with water, and the pore pressure and the evolution of pore volume during the experiments was not measured, the contribution of shear-enhanced compaction to pore fluid pressurization could not be modeled effectively.

The evolution of temperature T and pore pressure P were calculated by including the contributions of (i) the heat source from frictional heating, (ii) the heat sinks and pressure sources from dehydration and dehydroxylation of smectite, and from opal to quartz chemical reactions, and (iii) the pressure source from thermal pressurization. The evolution was described by the following coupled partial differential equations (Chen et al., 2013):

$$\frac{\partial T}{\partial t} = \frac{k}{\rho c}\frac{\partial^2 T}{\partial x^2} + \frac{\sum_i f_i}{\rho c} \tag{2}$$

$$\frac{\partial P}{\partial t} = \frac{K}{\eta S}\frac{\partial^2 P}{\partial x^2} + \frac{\sum_i F_i}{S} + \Lambda\frac{\partial T}{\partial t} \tag{3}$$

In equations (2) and (3), k is thermal conductivity (W/(m·K)), ρ is density (kg/m^3), c is heat capacity at constant pressure (J/(kg·K)), f_i represents the heat sources or sinks (W/m^3), K is permeability (m^2), η is viscosity of the pore fluid (Pa/s), S is specific storage (Pa^{-1}), F_i are the pressure sources (1/s), and Λ is the coefficient of thermal pressurization (Pa/K). The coefficient of thermal pressurization was calculated considering

Table 2
Input Parameters Used in the Numerical Model: Reaction Parameters

Name	i	$V_i(1)$ (%)	ΔH_i (kJ/mol)	$V_{f,i}$ (%)	A_i (1/s)	$E_{A,i}$
1W-0W dehydration	1	0 (vacuum dry, 150°C) 0.42 (vacuum dry, 100°C) 0.6 (room humidity, partly saturated)	−43 (2)	0.082 (2)	$1.9{\cdot}10^{16}$ (3)	132 (3)
dehydroxylation	2	0.6	−132 (2)	0.04 (2)	8.8 (2)	50.7 (2)
opal-CT to quartz	3	0.4	n.a.	0.1 (4)	2.3×10^{-3} (4)	66.9 (4)

(1) Calculated from time and temperature of pre heating (Ferrage et al., 2007), (2) Chen et al. (2013), and references therein, (3) Ferrage et al. (2007), and(4) Hüpers et al. (2017), and references therein.

measured porosity, thermal expansivity of pores at room conditions, and thermal expansivity of fluid with varying temperature and pressure (Rice, 2006). The heat source by frictional heating f_0 is

$$f_0 = \tau V/w \tag{4}$$

The shear strength evolution measured in the experiments was directly imported into the model, calculated from resisting torque assuming a constant stress acting on the gouge layer surface (Shimamoto & Tsutsumi, 1994). This assumption implies a constant and uniform pore fluid pressure along the gouge layer surface. The slip rate was set as a trapezoidal function with the same acceleration and deceleration as imposed in the experiments (6.4 m/s^2). Thickness w for each modeled experiment was constrained based on the microstructural evidence (see section 3.4).

Heat sinks (f_i) and pore pressure sources (F_i) were calculated for each of the possible chemical reactions, with $i = 1$ for smectite interlayer dehydration (the change from 1 water layer to 0 water layer configuration in the interlayer cation complex), $i = 2$ for smectite dehydroxylation, and $i = 3$ for the opal-CT to quartz reaction (Tables 2 and 3).

Heat sinks f_i and pore pressure sources F_i were

$$f_i = V_i(1-\varphi)\rho_s \Delta H_i / M_s \frac{\partial \xi_i}{\partial t} \tag{5}$$

$$F_i = V_i(1-\varphi)V_{f,i}\frac{\partial \xi_i}{\partial t} \tag{6}$$

with V_i the volume of solid reactant (in %), ΔH_i the reaction enthalpy (negative for the endothermic reactions presented here), ρ_s the density of solid reactant, M_s the molar mass of solid reactant, and $V_{f,i}$ the volume fraction of releasable fluid. The term $\partial\xi_i/\partial t$ is the time derivative of the reaction rate $\xi_i = 1 - exp(-t{\cdot}K_i)$:

$$\frac{\partial \xi_i}{\partial t} = K_i exp(-t\, K_i) \tag{7}$$

with K_i the Arrhenius term:

$$K_i = A_i\, exp\left(-E_{A,i}/R\, T\right) \tag{8}$$

for the preexponential rate of reaction A_i and the activation energy $E_{a,i}$ of the ith reaction (see Table 2).

Table 3
Input Parameters Used in the Numerical Model: Reaction Parameters: Thermal and Hydraulic Properties

		Φ (%)	K (m^2)	k_s (W/(m·K))	ρ_s (kg/m^3)	c_s (J/(kg·K))	S (Pa^{-1})
gouge layer	vacuum dry, 150°C vacuum dry, 100°C room humidity	0.4 (1)	10^{-16} (1)	1 (2)	2350 (2)	1000 (2)	$f(T,P)$ (3)
	partly saturated	0.35 (1)	10^{-21} (4)				
host rock	steel	0.04 (1*)	10^{-21} (1*)	44.5 (5)	7850 (5)	475 (5)	5.2×10^{-12} (5)

(1) Results of this paper, (1*) assumed in this paper, (2) Plotze et al. (2007), (3) Lemmon et al. (2002), (4) Behnsen and Faulkner (2011), and (5) Comsol Multiphysics materials library.

The smectite volume fraction in the starting material was assumed equal to the mass fraction (wt %) determined from XRD analysis due to the small density difference between smectite and opal-CT (see section 3.3 and Table 2). Because the temperature and the time duration in the oven for preheating (see section 2.1) affect the amount of interlayer cations with one water layer available for dehydration, the volume V_1 in smectite-rich gouges was estimated to be 0 wt % (with preheating at 150 °C for 24 hr) and in 42 wt % (with preheating at 100 °C for 12 hr) based on the method suggested by Ferrage et al. (2007) (Table 2). Regarding the other two reactions, dehydroxylation for smectites and quartz transition for opal-CT, the assumption made was that 100 wt % of both smectite and opal-CT could react.

The two partial differential equations (equations (2) and (3)) were solved with Comsol Multiphysics software. The equations were solved numerically as a one-dimensional problem: the x axis was in the direction perpendicular to the gouge layer basal boundary (Figures 1c and 1d). A total of 235 model nodes were organized as follows: 21 nodes, spaced every 0.0001 m ($0.5001 < x < 0.502$ m) defined the gouge layer domain, and the remaining 214 nodes, spaced every 0.005 m ($0 < x < 0.5$ m and $0.502 < x < 1.002$ m) defined the sample holder domain. In the first and last node (x = 0 and 1.002 m, respectively), we applied the Dirichelet boundary conditions of constant temperature and pressure equal to the initial temperature and pressure. The choice, in the model, of a very large sample holder domain prevented the boundary conditions from affecting the results and in particular to limit the temperature and pressure increase in the longer in duration (approximately 3,000 s) experiments performed at 0.001 m/s. The time step of the model decreased from 1 to 0.5, 0.1, and 0.01 s with increasing slip rate of the experiment.

For the gouge layer domain, thermal conductivity, density, and heat capacity were averaged as $X_{avg} = X_f\varphi + X_s(1-\varphi)$, with X_f the relative fluid property (which varied in the model with temperature from 295 to 1195 K and with pressure from 10^{-2} to 5×10^6 Pa (Lemmon et al., 2002), X_s the solid property at room temperature and pressure, and φ the porosity estimated with the gouge layer thickness before the experiments (section 3 and Table 3). Permeability was set constant with slip using the value measured for the gouges recovered from the vacuum dry and room humidity experiments (i.e., 10^{-17} m^2; section 3.1), and considering the value reported by Behnsen and Faulkner (2013) for gouges sheared under partly saturated conditions (Table 3). Specific storage was calculated as $S = \beta_b + \varphi\beta_f(1+\varphi)\beta_m$ with bulk compressibility β_b, mineral compressibility β_m (from Chen et al., 2013), and fluid compressibility β_f varying with temperature and pressure (Lemmon et al., 2002). Notably, in the models discussed here, the fluid properties varied with pressure and temperature considering implicitly the liquid or vapor state of water. For the sample holder domain the thermal conductivity, density and heat capacity of steel were used (Table 3). Porosity and permeability were assumed equal to 4% and 10^{-21} m^2, respectively, and specific storage was calculated from steel bulk compressibility (Table 3).

The microstructural analysis of deformed gouge layers showed intense deformation and comminution over their entire thickness when sheared at slip rates of 0.001, 0.01, and 0.1 m/s and strain localization when sheared at 1.3 m/s (SEM investigations; Figure 5). Therefore, the heat source f_0 was located in all the nodes of the gouge layer and over a thickness $w = 0.002$ m (= entire gouge layer) in the modeling of the low slip rate experiments (Figures 1d, 4, and 5). Instead, the heat source was located in one node point at the contact between the gouge layer and the sample holder (x = 0.5001 m; red circle in Figure 1d) and thickness w was set to 25 μm (extreme documented strain localization) for the experiments performed at 1.3 m/s (Figures 1d, 4, and 5).

Starting temperature was set to 25 °C for all the modeled experiments. Starting pore pressure was set to (i) the measured pressure of 10^{-8} MPa in the sample chamber during vacuum dry experiments, (ii) a pressure of 1.6×10^{-3} MPa during room humidity experiments (coinciding with 50% relative humidity in the sample chamber, that is, 50% of the water liquid-vapor saturation pressure at 25 °C), and (iii) the assumed pressure of 0.1 MPa in the partly saturated experiments. In cases (i) and (ii), the pore pressure was lower than the water liquid-vapor saturation pressure at 25 °C.

4.1.1. Results of the Numerical Model

The evolution of temperature, pressure, and reacted fraction for the thermochemical reactions with time are presented in Figure 6. These values are referred to a node of the model at the contact between the gouge layer and the sample holder domains (x = 0.5001 m; Figure 1d). As expected, according to the models, the temperature increased (i) with increasing target slip rate of the experiment and (ii) with decreasing water content in the gouge layer (i.e., from partly saturated to room humidity and vacuum dry conditions; Figures 6a–6d).

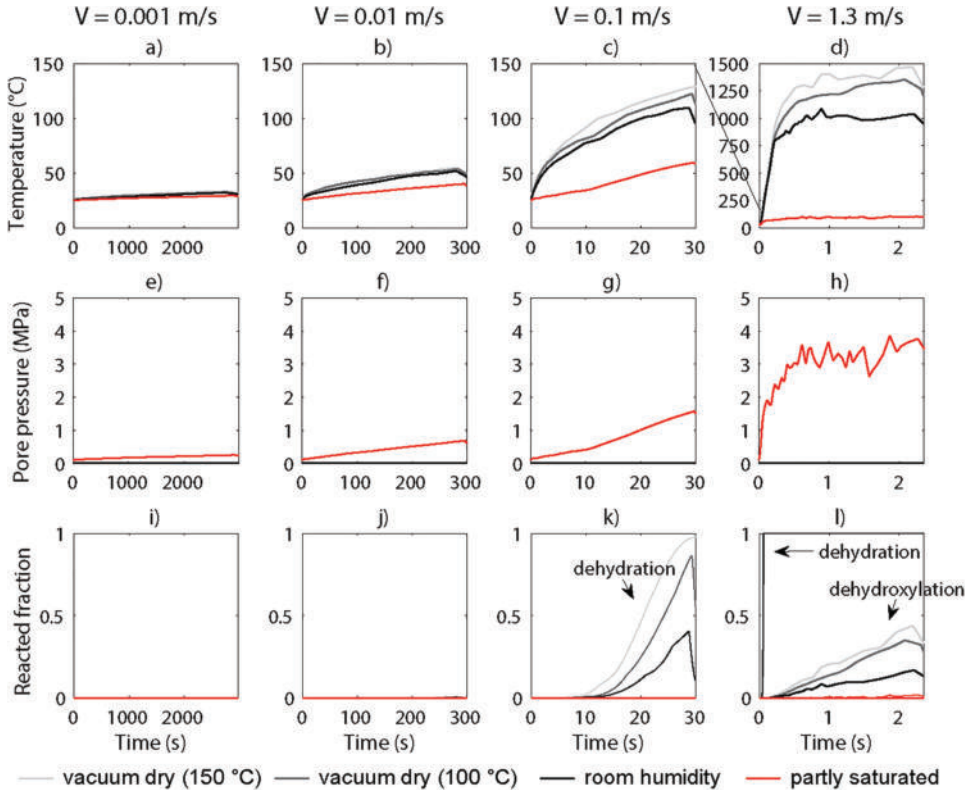

Figure 6. Modeling results: (a–d) the evolution of temperature, (e–h) pore pressure, and (i–l) the reacted fraction for dehydration and dehydroxylation with time in a point placed at the edge of the heat source (x = 0.5001 m; see Figure 1d). Each column represents all the starting materials deformed at the same slip rate of 0.001, 0.01, 0.1, and 1.3 m/s, respectively.

Pore pressure increased only in the partly saturated experiments and for slip rates ≥0.01 m/s (Figures 6e–6h). The maximum pore pressure increase occurred at 1.3 m/s (Figure 6h). The reacted fractions displayed a complex dependence on temperature, time, slip rate, and water content of the experiment (Figures 6i–6l). According to the models, the interlayer dehydration reaction was never completed in the experiments performed under partly saturated conditions and V = 0.001–0.01 m/s. Despite this incompleteness, at V = 0.1 m/s the amount of dehydrated smectite increased with decreasing initial water content in the gouge layer (i.e., from room humidity to vacuum dry conditions). Instead, at 1.3 m/s, dehydration was completed in approximately 100 ms (i.e., at the very beginning of the experiment). Lastly, dehydroxylation occurred only in the experiments performed at 1.3 m/s under room humidity and vacuum dry experiments and the fraction of decomposed smectite increased with the decreasing water content in the gouge layer. According to the models, the opal-CT to quartz reaction should not occur in the experimental conditions investigated in this study.

The roles played by (i) water availability in the gouge layers (i.e., whether gouges were preheated, at atmospheric humidity or with added liquid water) and (ii) initial pressure (i.e., room pressure or evacuated), on the temperature and pressure evolution (obtained by the models) during shearing and therefore on the activated deformation processes are discussed by reference to pressure-temperature-time (*P-T-t*) path diagrams (Figure 7). Smectite-rich gouge layers deformed under water-poor conditions (preheated vacuum dry to room humidity) follow a nearly adiabatic path within the water vapor field. In fact, with decreasing water content in the gouge layer and with increasing slip rate of the experiment, the *P-T-t* path simply progrades to higher temperatures with negligible pore pressure increase (Figure 7b). On the contrary, the *P-T-t* path of partly saturated experiments lies well within the liquid water field (Figures 7a and 7b). The results of the numerical model suggest that the pore pressure did not increase when the reacted fractions were maximum, excluding a role for thermochemical pressurization in controlling dynamic weakening in the

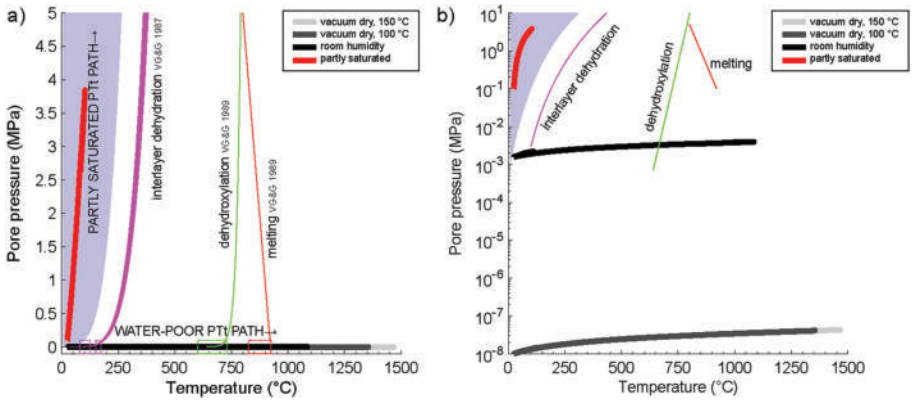

Figure 7. *Pp-T-t* path during the rotary shear experiments. Pore pressure versus temperature in (a) linear scale and (b) logarithmic scale to enhance the pore pressure evolution at the ultralow pressures of vacuum dry experiments. The stability field of liquid water is included as blue shaded area. Ca-montmorillonite-rich Wyoming bentonite interlayer dehydration (Van Groos & Guggenheim, 1987), dehydroxylation, and melting (Van Groos & Guggenheim, 1989) reactions are included in the plots (purple area, green, and red line, respectively). Boxes indicate dehydration, dehydroxylation, and melting reactions at room pressure and temperature of exactly the same material that was tested in our experiments, STx-1b (Guggenheim & Van Groos, 2001).

case of both dry and partly saturated experiments. In fact, the reacted products from dehydration were maximum in the 1.3-m/s room humidity and vacuum dry experiments when the pore pressure rise was negligible (Figure 6l) and were always zero when the pore pressure increased in the partly saturated experiments (Figures 6e–6h with Figures 6i–6l). A possible explanation for the negligible role for thermochemical pressurization in the dry experiments was that the pore fluid at low pore fluid pressure had a large pore fluid compressibility which strongly reduced the specific storage. In fact, in vacuum dry and room humidity experiments (pore pressures of 10^{-8} and 10^{-3} MPa, respectively), the compressibility of water vapor (β_f of approximately 100 and 10^{-4} Pa, respectively) was several orders of magnitude larger compared to the compressibility of liquid water in partly saturated experiments (β_f of approximately 10^{-10} Pa). This resulted in a lower specific storage and reduced the pore pressure source terms (see equation (3)). At the same time, the lower temperatures achieved in the partly saturated experiments due to the lower frictional strength of the materials did not allow the chemical reactions to advance despite the liquid water compressibility (and thus the specific storage) allowing for a pore pressure increase.

The results of the numerical models also show that the liquid-vapor transition was not crossed during the partly saturated experiments. Under partly saturated conditions, the calculated temperature was lower than the 100 °C required at 0.1 MPa of pore fluid pressure to result in water vaporization. Moreover, because of the pressurization of pore fluids and because of the liquid-vapor saturation temperature increase with pressure, the temperature increase required to induce the phase transition had to increase as well making the vaporization process less likely to occur.

4.2. Deformation Processes Activated in the Experiments

The interpretation of the numerical model results and their combination with the experimental, mineralogical, and microstructural observations suggest that pore fluid thermochemical pressurization did not occur under vacuum dry and room humidity conditions and therefore the evolution of shear strength depended mainly on the friction coefficient of the smectite-rich gouge. On the other hand, under partly saturated conditions, mechanical, and thermal pore fluid pressurization occurred, and shear strength evolution depended on both pore pressure and friction coefficient.

4.2.1. Deformation Processes in Vacuum Dry and Room Humidity Experiments (Water-Poor Conditions)

In water-poor conditions, the friction coefficient was controlled by extreme grain size reduction which, with increasing slip rate and strain localization, led to thermal decomposition and melting at coseismic slip rates (>1 m/s; Figures 4 and 5). In particular, the lower the water content, the higher the temperatures achieved in the gouge layer and the dehydration and dehydroxylation reactions advanced until bulk melting occurred.

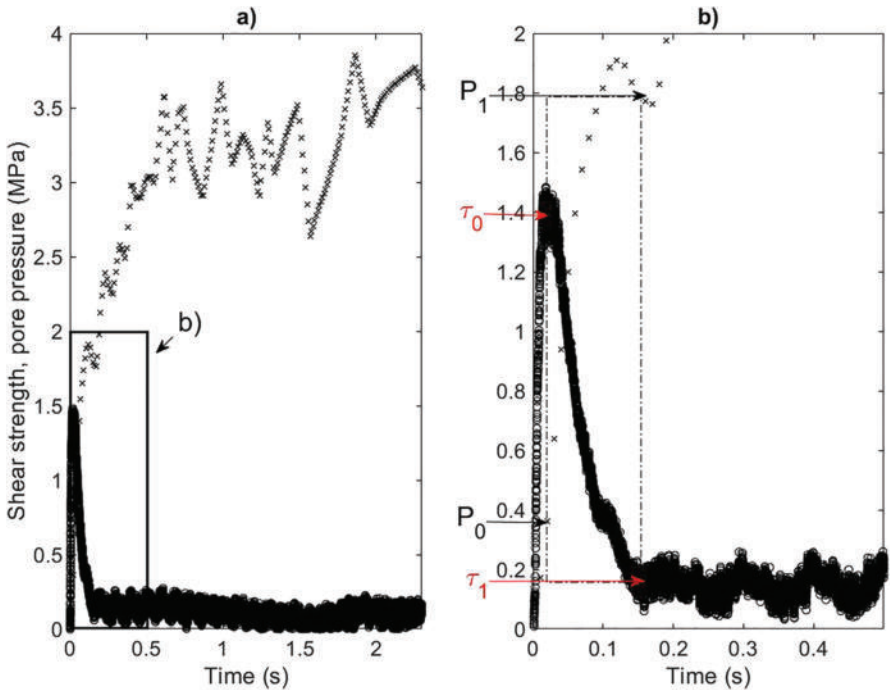

Figure 8. Measured shear strength and modeled pore fluid pressure in water partly saturated experiments. (a) The experiment s1251 was run at 1.3 m/s under partly saturated conditions. (b) The initial part of slip weakening stage 1 of the experiment. The symbols of equation (9) are indicated in the plot.

The presence of nanoparticles (but no evidence of melting) in the room humidity experiments and of pseudotachylytes in the vacuum dry experiments (Figure 5c) and the modeled temperatures (Figure 6d) in excess of the smectite dehydroxylation (500–700 °C; Van Groos & Guggenheim, 1989) and melting (830 °C; Guggenheim & Van Groos, 2001) are consistent with this interpretation. At seismic slip rates of 1.3 m/s, the combination of strain localization and frictional power density (>1.6 MW/m^2 under room humidity and >2 MW/m^2; Table 1) drove the temperatures up and led to dynamic weakening. In the room humidity case, the process producing dynamic weakening could be grain size-dependent grain boundary sliding in the nanoparticles domains produced either by grain size reduction or by thermal decomposition (De Paola et al., 2015; Green et al., 2015). In the vacuum-dry case, the process producing dynamic weakening was likely frictional melting (Figure 2d). At slip rates of 0.001–0.1 m/s, extreme grain size reduction occurred (i.e., ultracomminuted bands in Figure 5 and in Aretusini et al. (2017)), but strain localization did not occur and frictional power density was low (0.003–0.3 MW/m^2; Table 1). As a consequence, temperatures achieved in the gouge layer were not high enough to promote either grain size-dependent crystal plastic processes or frictional melting and large dynamic weakening did not occur (Figures 2a–2c).

4.2.2. Deformation Processes in Partly Saturated Experiments (Water-Rich Conditions)

To assess the role of the modeled pore pressures induced by thermal pressurization (Figure 6h) in dynamic weakening during stage 1 (Figures 2a–2d), we consider the ratio between the shear strength at the end and the shear strength at the onset of the slip weakening stage 1 (cf. Violay et al., 2015), expressed as

$$\frac{\tau_1}{\tau_0} = \frac{\mu_1\,(\sigma_n - P_1)}{\mu_0(\sigma_n - P_0)} \tag{9}$$

wherein τ_0 is the peak strength, τ_1 is the strength at the end of slip weakening, μ_0 and μ_1 are the respective friction coefficients, P_0 and P_1 are the respective pore fluid pressures calculated in the numerical model, and σ_n is the total normal stress (5 MPa; Figure 8). It suggested that the pore pressure rise by thermal pressurization alone could not control the short-duration dynamic weakening. In fact, dynamic weakening could be explained either by a friction coefficient decrease (at constant pressure $P_1 = P_0$) or by an additional pore

pressure term. In the second case, we can assume that the friction coefficient was constant and solve the equation:

$$\frac{\tau_1}{\tau_0} = \frac{\sigma_n - (P_0 + \Delta P_x)}{\sigma_n - P_0} \tag{10}$$

for an unknown ΔP_x pore fluid pressure increase which can possibly arise from thermal pressurization. This term ΔP_x was 4.3 MPa with slip rate of 1.3 m/s to justify the dynamic weakening recorded in the experiment. In the case of experiment s1251 run at 1.3 m/s (Figure 8), the pore pressure increase was only approximately 1.4 MPa, thus significantly smaller than the 4.3 MPa needed to achieve dynamic weakening by thermal pressurization only. This implies that either a decrease of the effective friction coefficient or an additional pressurization term (e.g., by compaction with shear deformation) is necessary to explain dynamic weakening during stage 1.

A combination of friction coefficient increase and pore pressure decrease could result in the slip strengthening behavior measured in the experiments at $V = 0.001$–0.1 m/s (Figures 2a–2c). Slip strengthening could occur by a decrease of pore pressure or by an increase in the friction coefficient. However, according to the results of the model, during stage 2 both the thermal and shear-enhanced components of pore fluid pressure should increase. On the other hand, the poor sealing of the gouge layer would allow a loss of water resulting in the decrease of pore pressure and, as a consequence, higher shear strength. Moreover, the temperature increase associated with frictional heating would induce water loss and dehydration from the smectite interlayers and grain boundaries, resulting in a less efficient lubrication of the smectite interfaces and thus a bulk increase of the friction coefficient.

4.2.3. Origin of the Amorphous Material

In the experiments, the production of amorphous materials was favored at low temperatures, low slip velocities, and under room humidity compared to the partly saturated conditions (i.e., when strain did not localize in the gouge layer; Aretusini et al., 2017). In the room humidity experiments, an increase of the amount of amorphous material was measured in all the studied gouges, independently of imposed the slip rate. The shear bands contained amorphous material in the form of smectite nanoparticles (Figures 5a and 5b; see also Aretusini et al., 2017), similar in shape to those produced in the high-energy ball milling experiments (Dellisanti & Valdré, 2005; Vdović et al., 2010). In the partly saturated experiments amorphous material was produced but not in the form of nanoparticles (absent in these experiments). Alternatively, the increase of amorphous material could derive from the mechanical breakdown of the smectite crystals, for example, by delamination along the basal surfaces (Table 1 and Figure 3c). Limited to the room humidity and partly saturated experiments, the amorphous material was not associated with microstructural evidences of frictional melting (i.e., pseudotachilyte) and was possibly derived from mechanical alteration of the smectite lattice, promoting solid state amorphization (cf. Aretusini et al., 2017).

4.3. Markers of Fast Accelerated Slip in Natural Rocks

The high-velocity friction experiments presented here were representative of fast slip during either seismic slip propagation (average of 1 m/s) or during the final collapse of a landslide (higher than 10 m/s). The applied normal stresses almost reproduced the low effective normal stresses typical of smectite-rich sections of seismogenic megathrust faults, as in the Japan Trench (7 MPa; Fulton et al., 2013), and of large landslides (4.9 MPa for Vajont 1963 landslide; Veveakis et al., 2007). Given the similarity in slip rate values between the experiments and the natural events, the microstructures analyzed in the experiments might be used to recognize diagnostic features of either fast (seismic) or slow (aseismic) slip occurred in natural faults or landslides and constrain the deformation processes occurring in nature. Fast slip rates (>0.1 m/s) result in the dissipation within the slip zone of frictional power densities (i.e., the product of slip rate and shear stress) typically higher than 10^{-2} MW/m^2. Given the low thermal conductivity of rocks, the dissipated frictional power induces a temperature rise in the slip zone which activates deformation processes characteristic of seismic slip or accelerated landslide collapse. In general, these processes (thermo-poro-mechanical pressurization, melt lubrication, crystal plastic grain-size- and temperature-dependent deformation mechanisms, etc.) determine dynamic weakening of the slip zone (Di Toro et al., 2011; Green et al., 2015; Rice, 2006; Rowe et al., 2019).

Recent high-velocity friction experimental studies tried to recognize microstructural markers from rocks or gouges deformed at fast slip rates (1 m/s) that, when found in natural rocks, could indicate past seismic slip or accelerated landslide collapse (Niemeijer et al., 2012; Rowe & Griffith, 2015). The least ambiguous markers of fast slip are surely pseudotachylites resulting from frictional melting, as documented in natural fault rocks (Sibson, 1975) and landslide décollements (Legros et al., 2000). In the case of clay-rich fault gouges, pseudotachylites were proposed as markers of fast slip at shallow depth (Han et al., 2014). However, the scarcity of pseudotachylytes in the geological record motivated the search for other markers of fast slip. These include clay clast aggregates (CCAs, Boutareaud et al., 2008), transformed clay minerals (Bullock et al., 2014; Ferri et al., 2011; Yamaguchi et al., 2011), or nanoparticles aggregated in fibers (Smeraglia et al., 2017), although these "markers" of ancient seismic slip are still regarded as debatable.

To compare our experimental findings with (1) the microstructures produced in previous experiments performed on clay-rich gouges and in natural slip zones and (2) the proposed deformation mechanisms, we need to consider that the frictional power density and therefore the temperature rise increases with the shear stress and, therefore, with the normal stress imposed in the experiment or achieved in nature. Compared to previous experimental configurations, the average frictional power density dissipated in the slip zone of our experiments (0.15 to 2.24 MW/m^2) is up to 5 times higher (Boulton et al., 2017; Boutareaud et al., 2008; Brantut et al., 2008; Ferri et al., 2011; French et al., 2014), comparable (Han et al., 2014; Remitti et al., 2015) or lower (Bullock et al., 2015; Smeraglia et al., 2017). The higher frictional power density dissipated in our experiments can explain the higher maximum temperatures achieved compared to published data (for example in French et al., 2014). Moreover, we need to consider the role of thermal diffusivity: the low diffusivity typical of host rocks in nature compared to the higher one of the steel-made holder used in this study promotes the increase of temperature and dynamic weakening during slip (Yao et al., 2016). In conclusion, further experimental and numerical modeling work is required for a direct and systematic comparison of our results with the available ones.

In our experiments, if the water content remains constant, almost identical microstructural products occur at all slip rates from 0.001 to 1.3 m/s, that is, nanoparticles in room humidity or nanofoliations in partly saturated experiments (Aretusini et al., 2019). In the room humidity case, clay clast aggregates were produced in a broad range of slip rate and frictional power densities. These observations question the role of CCAs as reliable markers of fast accelerated slip in smectite-rich rocks as discussed in Boutareaud et al. (2008) and, instead, agree with the observation of CCAs as a common product from shear of dry gouges at low normal stresses (of calcitic composition in the case of Rempe et al. (2014)). Similarly as CCAs, nanoparticles in our experiments were produced over a broad range of slip rates and frictional power densities. However, highly localized deformation in nanoparticles domains could be indicative of seismic slip (Aretusini et al., 2017; Smeraglia et al., 2017) and strain localization can be controlled by thermal decomposition processes (French & Chester, 2018). In presence of water (partly saturated experiments), highly localized (<150 μm thick) nanofoliated gouge volumes could be indicative of seismic slip (Aretusini et al., 2019) and compatible with strain localization controlled by thermal pressurization (French & Chester, 2018).

In our experiment performed on the gouge preheated at 100 °C, under high vacuum, and sheared at 1.3 m/s, a pseudotachylite developed (Figure 5c), which is considered a reliable marker of fast accelerated slip. However, the pseudotachylite developed under conditions of water depletions very far from those expected at shallow depth in natural faults and landslide décollements, where water is available in pore spaces and inside smectite lattice. This pseudotachylite formed in the experiments with the highest average power density (>2 MW/m^2; Table 1), whereas with water available, a foliation developed with a lower average power density (approximately 0.15 MW/m^2; Table 1). Therefore, in presence of water, to achieve frictional melting, a frictional power 15 times larger than those we measured is required. To increase frictional power, the product of shear stress and the slip rate of the slip pulse have to increase (section 2.3). At shallow depth, at the normal stress of our experiments, higher slip rates than in our experiments are required to achieve a higher power density. At greater depth, higher shear stresses promote a higher power density. Moreover, at large depth, the higher temperatures due to the geothermal gradient could promote dehydrated smectites which were shown to have a shear stress approximately 5 times the one of water saturated smectites (i.e., at normal stress of 100 MPa; Morrow et al., 2017).

5. Conclusions

Rotary shear experiments were conducted on smectite-rich gouges containing 70 wt % Ca-montmorillonite and 30 wt % opal-CT. Gouges layers were deformed under water-poor (vacuum dry and room humidity) and partly saturated conditions. The 2-mm-thick gouge layers were deformed by imposing the same normal stress (5 MPa) and total displacement (3 m), but at slip rates of 0.001, 0.01, 0.1, and 1.3 m/s (Table 1 and Figure 2). By incorporating the mechanical data (Figure 2) into a thermochemical and thermal pressurization *P-T* model (Figure 6) and constraining the model results with microstructural (Figures 4 and 5) and mineralogical (Figure 3) evidence, we conclude that

1. Water-poor (vacuum dry and room humidity) conditions promote cataclasis and solid amorphization, dehydration (release of interlayer water molecules) and, with fast slip rate and high frictional power, dehydroxylation (release of hydroxyls) and frictional melting. Development of high pore fluid pressures (thermochemical pressurization) is hindered by the vapor state of water and deformation occurs under quasi adiabatic conditions.
2. Water-rich (or partly saturated) conditions promoted frictional slip associated with shear enhanced pressurization and, for $V = 0.01–1.3$ m/s, with thermal pressurization. Vaporization of pore water was not expected to occur at the experimental conditions discussed here.
3. The experiments are representative of the ambient pressure and temperature conditions typical of the shallow sections of megathrust fault zones (e.g., Tohoku-Oki 2011 M_w 9.0 earthquake; Fulton et al., 2013) or of landslides décollements (e.g., Vajont 1963; Hendron & Patton, 1987).
4. In the above shallow geological environments, markers of fast slip associated with earthquakes and landslides should be difficult to recognize based on the microstructures found in the slipping zones, as the products of deformation are nonexclusive of fast slip rates (nanoparticles, CCAs, and nanofoliation).
5. Pseudotachylites in smectite-rich rocks are product of seismic faulting or accelerated landslides only with high frictional power (>2 MW/m^2), which can be achieved at shallow depth with a combination of fast slip and high displacement, or at higher depth thanks to the higher normal stresses and strengthening with dehydration during diagenesis and burial.

Acknowledgments
This work was supported by the European Research Council Consolidator Grant Project 614705 NOFEAR. We thank J. Mecklenburgh for the help and advice in the permeability data reduction. We thank E. Trasatti for the access to Comsol Multiphysics software. We thank two anonymous reviewers and the Editor for their constructive comments that allowed us to improve this study. The experimental data supporting this study are publicly available online (Di Toro & Aretusini, 2019).

References

Aretusini, S., Mittempergher, S., Plümper, O., Spagnuolo, E., Gualtieri, A. F., & Di Toro, G. (2017). Production of nanoparticles during experimental deformation of smectite and implications for seismic slip. *Earth and Planetary Science Letters*, *463*, 221–231. https://doi.org/10.1016/j.epsl.2017.01.048

Aretusini, S., Plümper, O., Spagnuolo, E., & Toro, G. D. (2019). Subseismic to Seismic Slip in Smectite Clay Nanofoliation. *Journal of Geophysical Research: Solid Earth*, *124*, 6589–6601. https://doi.org/10.1029/2019JB017364

Behnsen, J., & Faulkner, D. R. (2011). Water and argon permeability of phyllosilicate powders under medium to high pressure. *Journal of Geophysical Research*, *116*, B12203. https://doi.org/10.1029/2011JB008600

Behnsen, J., & Faulkner, D. R. (2013). Permeability and frictional strength of cation-exchanged montmorillonite. *Journal of Geophysical Research: Solid Earth*, *118*, 2788–2798. https://doi.org/10.1002/jgrb.50226

Bergmann, J., Friedel, P., & Kleeberg, P. (1998). BGMN - a new fundamental parameters based rietveld program for laboratory x-ray sources, its use in quantitative analysis and structure investigations. In *CPD Newsletter* (Vol. 20, pp. 5–8).Commission of Powder Diffraction, International Union of Crystallography.

Bernabé, Y., Mok, U., & Evans, B. (2006). A note on the oscillating flow method for measuring rock permeability. *International Journal of Rock Mechanics and Mining Sciences*, *43*(2), 311–316. https://doi.org/10.1016/j.ijrmms.2005.04.013

Boulton, C., Yao, L., Faulkner, D. R., Townend, J., Toy, V. G., Sutherland, R., et al. (2017). High-velocity frictional properties of Alpine Fault rocks: Mechanical data, microstructural analysis, and implications for rupture propagation. *Journal of Structural Geology*, *97*, 71–92. https://doi.org/10.1016/j.jsg.2017.02.003

Boutareaud, S., Calugaru, D.-G., Han, R., Fabbri, O., Mizoguchi, K., Tsutsumi, A., & Shimamoto, T. (2008). Clay-clast aggregates: A new textural evidence for seismic fault sliding? *Geophysical Research Letters*, *35*, L05302. https://doi.org/10.1029/2007GL032554

Brantut, N., Schubnel, A., Rouzaud, J.-N., Brunet, F., & Shimamoto, T. (2008). High-velocity frictional properties of a clay-bearing fault gouge and implications for earthquake mechanics. *Journal of Geophysical Research*, *113*, B10401. https://doi.org/10.1029/2007JB005551

Bullock, R. J., De Paola, N., & Holdsworth, R. E. (2015). An experimental investigation into the role of phyllosilicate content on earthquake propagation during seismic slip in carbonate faults. *Journal of Geophysical Research: Solid Earth*, *120*, 3187–3207. https://doi.org/10.1002/2015JB011914

Bullock, R. J., De Paola, N., Holdsworth, R. E., & Trabucho-Alexandre, J. (2014). Lithological controls on the deformation mechanisms operating within carbonate-hosted faults during the seismic cycle. *Journal of Structural Geology*, *58*, 22–42. https://doi.org/10.1016/j.jsg.2013.10.008

Carpenter, B. M., Marone, C., & Saffer, D. M. (2011). Weakness of the San Andreas Fault revealed by samples from the active fault zone. *Nature Geoscience*, *4*(4), 251–254. https://doi.org/10.1038/ngeo1089

Chen, J., Niemeijer, A., Yao, L., & Ma, S. (2017). Water vaporization promotes coseismic fluid pressurization and buffers temperature rise: VAPORIZATION OF FAULT WATER. *Geophysical Research Letters*, *44*, 2177–2185. https://doi.org/10.1002/2016GL071932

Chen, J., Niemeijer, A. R., & Fokker, P. A. (2017). Vaporization of fault water during seismic slip: Earthquake-Induced Vaporization. *Journal of Geophysical Research: Solid Earth*, *122*, 4237–4276. https://doi.org/10.1002/2016JB013824

Chen, J., Yang, X., Duan, Q., Shimamoto, T., & Spiers, C. J. (2013). Importance of thermochemical pressurization in the dynamic weakening of the Longmenshan Fault during the 2008 Wenchuan earthquake: Inferences from experiments and modeling. *Journal of Geophysical Research: Solid Earth*, *118*, 4145–4169.

Chen, J., Yang, X., Yao, L., Ma, S., & Shimamoto, T. (2013). Frictional and transport properties of the 2008 Wenchuan Earthquake fault zone: Implications for coseismic slip-weakening mechanisms. *Tectonophysics*, *603*, 237–256. https://doi.org/10.1016/j.tecto.2013.05.035

Chipera, S. J., & Bish, D. L. (2001). Baseline studies of the clay minerals society source clays: powder X-ray diffraction analyses. *Clays and Clay Minerals*, *49*(5), 398–409. https://doi.org/10.1346/CCMN.2001.0490507

David, C., Wassermann, J., Amann, F., Klaver, J., Davy, C., Sarout, J., et al. (2018). KG^2B, a collaborative benchmarking exercise for estimating the permeability of the Grimsel granodiorite—Part 2: modelling, microstructures and complementary data. *Geophysical Journal International*, *215*(2), 825–843. https://doi.org/10.1093/gji/ggy305

De Paola, N., Holdsworth, R. E., Viti, C., Collettini, C., & Bullock, R. (2015). Can grain size sensitive flow lubricate faults during the initial stages of earthquake propagation? *Earth and Planetary Science Letters*, *431*, 48–58. https://doi.org/10.1016/j.epsl.2015.09.002

Dellisanti, F., & Valdré, G. (2005). Study of structural properties of ion treated and mechanically deformed commercial bentonite. *Applied Clay Science*, *28*(1-4), 233–244. https://doi.org/10.1016/j.clay.2003.12.036

Di Toro, G., & Aretusini, S. (2019). High velocity friction data and thermochemical modeling data of smectite-rich STx-1b (vacuum dry, room humidity and water partly saturated). https://doi.org/10.25430/researchdata.cab.unipd.it.00000134

Di Toro, G., Han, R., Hirose, T., De Paola, N., Nielsen, S., Mizoguchi, K., et al. (2011). Fault lubrication during earthquakes. *Nature*, *471* (7339), 494–498. https://doi.org/10.1038/nature09838

Di Toro, G., Niemeijer, A., Tripoli, A., Nielsen, S., Di Felice, F., Scarlato, P., et al. (2010). From field geology to earthquake simulation: a new state-of-the-art tool to investigate rock friction during the seismic cycle (SHIVA). *Rendiconti Lincei*, *21*(S1), 95–114. https://doi.org/10.1007/s12210-010-0097-x

Doebelin, N., & Kleeberg, R. (2015). Profex: a graphical user interface for the Rietveld refinement program BGMN. *Journal of Applied Crystallography*, *48*(5), 1573–1580. https://doi.org/10.1107/S1600576715014685

Faulkner, D. R., Mitchell, T. M., Behnsen, J., Hirose, T., & Shimamoto, T. (2011). Stuck in the mud? Earthquake nucleation and propagation through accretionary forearcs. *Geophysical Research Letters*, *38*, L18303. https://doi.org/10.1029/2011GL048552

Faulkner, D. R., Sanchez-Roa, C., Boulton, C., & den Hartog, S. A. M. (2018). Pore Fluid Pressure Development in Compacting Fault Gouge in Theory, Experiments, and Nature. *Journal of Geophysical Research: Solid Earth*, *123*, 226–241. https://doi.org/10.1002/2017JB015130

Ferrage, E., Kirk, C. A., Cressey, G., & Cuadros, J. (2007). Dehydration of Ca-montmorillonite at the crystal scale. Part 2. Mechanisms and kinetics. *American Mineralogist*, *92*(7), 1007–1017. https://doi.org/10.2138/am.2007.2397

Ferri, F., Di Toro, G., Hirose, T., Han, R., Noda, H., Shimamoto, T., et al. (2011). Low- to high-velocity frictional properties of the clay-rich gouges from the slipping zone of the 1963 Vaiont slide, northern Italy. *Journal of Geophysical Research*, *116*, B11298. https://doi.org/10.1029/2011JB008338

Ferri, F., Di Toro, G., Hirose, T., & Shimamoto, T. (2010). Evidence of thermal pressurization in high-velocity friction experiments on smectite-rich gouges: Thermal pressurization of clay-rich gouges. *Terra Nova*, *22*(5), 347–353. https://doi.org/10.1111/j.1365-3121.2010.00955.x

French, M. E., & Chester, J. S. (2018). Localized Slip and Associated Fluidized Structures Record Seismic Slip in Clay-Rich Fault Gouge. *Journal of Geophysical Research: Solid Earth*, *123*, 8568–8588. https://doi.org/10.1029/2018JB016053

French, M. E., Kitajima, H., Chester, J. S., Chester, F. M., & Hirose, T. (2014). Displacement and dynamic weakening processes in smectite-rich gouge from the Central Deforming Zone of the San Andreas Fault. *Journal of Geophysical Research: Solid Earth*, *119*, 1777–1802. https://doi.org/10.1002/2013JB010757

Fulton, P. M., Brodsky, E. E., Kano, Y., Mori, J., Chester, F., Ishikawa, T., et al., & Expedition 343, 343T, and KR13-08 Scientists (2013). Low Coseismic Friction on the Tohoku-Oki Fault Determined from Temperature Measurements. *Science*, *342*(6163), 1214–1217. https://doi.org/10.1126/science.1243641

Gosman, A. L., McCarty, R. D., & Hust, J. G. (1969). Thermodynamic Properties of Argon from the Triple Point to 300 K at Pressures to 1000 Atmospheres, (No. NSRDS-NBS-27). NATIONAL STANDARD REFERENCE DATA SYSTEM, NATIONAL STANDARD REFERENCE DATA SYSTEM. Retrieved from http://www.dtic.mil/docs/citations/ADD095345

Green, H. W., Shi, F., Bozhilov, K., Xia, G., & Reches, Z. (2015). Phase transformation and nanometric flow cause extreme weakening during fault slip. *Nature Geoscience*, *8*(6), 484–489. https://doi.org/10.1038/ngeo2436

Gualtieri, A. F. (2000). Accuracy of XRPD QPA using the combined Rietveld–RIR method. *Journal of Applied Crystallography*, *33*(2), 267–278. https://doi.org/10.1107/S002188989901643X

Guggenheim, S., & Van Groos, A. K. (2001). Baseline Studies of the Clay Minerals Society Source Clays: Thermal Analysis. *Clays and Clay Minerals*, *49*(5), 433–443. https://doi.org/10.1346/CCMN.2001.0490509

Han, R., Hirose, T., Jeong, G. Y., Ando, J., & Mukoyoshi, H. (2014). Frictional melting of clayey gouge during seismic fault slip: Experimental observation and implications: Frictional melting of clayey gouge. *Geophysical Research Letters*, *41*, 5457–5466. https://doi.org/10.1002/2014GL061246

Hendron, A. J., & Patton, F. D. (1987). The Vaiont slide—a geotechnical analysis based on new geologic observations of the failure surface. *Engineering Geology*, *24*(1-4), 475–491. https://doi.org/10.1016/0013-7952(87)90080-9

Holdsworth, R. E., van Diggelen, E. W. E., Spiers, C. J., de Bresser, J. H. P., Walker, R. J., & Bowen, L. (2011). Fault rocks from the SAFOD core samples: Implications for weakening at shallow depths along the San Andreas Fault, California. *Journal of Structural Geology*, *33*(2), 132–144. https://doi.org/10.1016/j.jsg.2010.11.010

Hüpers, A., Torres, M. E., Owari, S., McNeill, L. C., Dugan, B., Henstock, T. J., et al. (2017). Release of mineral-bound water prior to subduction tied to shallow seismogenic slip off Sumatra. *Science*, *356*(6340), 841–844. https://doi.org/10.1126/science.aal3429

Ikari, M. J., Saffer, D. M., & Marone, C. (2007). Effect of hydration state on the frictional properties of montmorillonite-based fault gouge. *Journal of Geophysical Research*, *112*, B06423. https://doi.org/10.1029/2006JB004748

Kearey, P., Klepeis, K. A., & Vine, F. J. (2013). Continental transforms and strike-slip faults. *Global Tectonics* (pp. 210–248).

Kitajima, H., Chester, J. S., Chester, F. M., & Shimamoto, T. (2010). High-speed friction of disaggregated ultracataclasite in rotary shear: Characterization of frictional heating, mechanical behavior, and microstructure evolution. *Journal of Geophysical Research*, *115*, B08408. https://doi.org/10.1029/2009JB007038

Kuo, L.-W., Song, S.-R., Yeh, E.-C., & Chen, H.-F. (2009). Clay mineral anomalies in the fault zone of the Chelungpu Fault, Taiwan, and their implications. *Geophysical Research Letters*, *36*, L18306. https://doi.org/10.1029/2009GL039269

Legros, F., Cantagrel, J., & Devouard, B. (2000). Pseudotachylyte (Frictionite) at the Base of the Arequipa Volcanic Landslide Deposit (Peru): Implications for Emplacement Mechanisms. *The Journal of Geology*, *108*(5), 601–611. https://doi.org/10.1086/314421

Lemmon, E. W., Huber, M. L., & McLinden, M. O. (2002). NIST reference fluid thermodynamic and transport properties—REFPROP. *NIST Standard Reference Database*, *23*, v7.

McKernan, R., Mecklenburgh, J., Rutter, E., & Taylor, K. (2017). *Microstructural controls on the pressure-dependent permeability of Whitby mudstone*, *Special Publications* (Vol. 454). London: Geological Society. https://doi.org/10.1144/SP454.15

Michels, A., Botzen, A., & Schuurman, W. (1954). The viscosity of argon at pressures up to 2000 atmospheres. *Physica*, *20*(7–12), 1141–1148. https://doi.org/10.1016/S0031-8914(54)80257-6

Mizoguchi, K., Hirose, T., Shimamoto, T., & Fukuyama, E. (2007). Reconstruction of seismic faulting by high-velocity friction experiments: An example of the 1995 Kobe earthquake. *Geophysical Research Letters*, *34*, L01308. https://doi.org/10.1029/2006GL027931

Moore, D. E., & Lockner, D. A. (2007). Friction of the Smectite Clay Montmorillonite. In *The Seismogenic Zone of Subduction Thrust Faults* (pp. 317–345). New York: Columbia University Press.

Morrow, C. A., Moore, D. E., & Lockner, D. A. (2017). Frictional strength of wet and dry montmorillonite: Montmorillonite Strength. *Journal of Geophysical Research: Solid Earth*, *122*, 3392–3409. https://doi.org/10.1002/2016JB013658

Nakamura, S., Gibo, S., Egashira, K., & Kimura, S. (2010). Platy layer silicate minerals for controlling residual strength in landslide soils of different origins and geology. *Geology*, *38*(8), 743–746. https://doi.org/10.1130/G30908.1

Niemeijer, A., Di Toro, G., Griffith, W. A., Bistacchi, A., Smith, S. A. F., & Nielsen, S. (2012). Inferring earthquake physics and chemistry using an integrated field and laboratory approach. *Journal of Structural Geology*, *39*, 2–36. https://doi.org/10.1016/j.jsg.2012.02.018

Niemeijer, A., Di Toro, G., Nielsen, S., & Di Felice, F. (2011). Frictional melting of gabbro under extreme experimental conditions of normal stress, acceleration, and sliding velocity. *Journal of Geophysical Research*, *116*, B07404. https://doi.org/10.1029/2010JB008181

Oohashi, K., Hirose, T., Takahashi, M., & Tanikawa, W. (2015). Dynamic weakening of smectite-bearing faults at intermediate velocities: Implications for subduction zone earthquakes: Dynamic weakening of smectite faults. *Journal of Geophysical Research: Solid Earth*, *120*, 1572–1586. https://doi.org/10.1002/2015JB011881

Plötze, M., Kahr, G., Dohrmann, R., & Weber, H. (2007). Hydro-mechanical, geochemical and mineralogical characteristics of the bentonite buffer in a heater experiment: The HE-B project at the Mont Terri Rock Laboratory. *Physics and Chemistry of the Earth, Parts A/B/C*, *32*(8-14), 730–740.

Remitti, F., Smith, S. A. F., Mittempergher, S., Gualtieri, A. F., & Di Toro, G. (2015). Frictional properties of fault zone gouges from the J-FAST drilling project (Mw 9.0 2011 Tohoku-Oki earthquake). *Geophysical Research Letters*, *42*, 2691–2699. https://doi.org/10.1002/2015GL063507

Rempe, M., Smith, S. A. F., Ferri, F., Mitchell, T. M., & Di Toro, G. (2014). Clast-cortex aggregates in experimental and natural calcite-bearing fault zones. *Journal of Structural Geology*, *68*, 142–157. https://doi.org/10.1016/j.jsg.2014.09.007

Rice, J. R. (2006). Heating and weakening of faults during earthquake slip. *Journal of Geophysical Research*, *111*, B05311. https://doi.org/10.1029/2005JB004006

Rowe, C. D., & Griffith, W. A. (2015). Do faults preserve a record of seismic slip: A second opinion. *Journal of Structural Geology*, *78*, 1–26. https://doi.org/10.1016/j.jsg.2015.06.006

Rowe, C. D., Lamothe, K., Rempe, M., Andrews, M., Mitchell, T. M., Di Toro, G., et al. (2019). Earthquake lubrication and healing explained by amorphous nanosilica. *Nature Communications*, *10*, 320. https://doi.org/10.1038/s41467-018-08238-y

Rutter, E. H., Maddock, R. H., Hall, S. H., & White, S. H. (1986). Comparative microstructures of natural and experimentally produced clay-bearing fault gouges. *Pure and Applied Geophysics*, *124*(1–2), 3–30. https://doi.org/10.1007/BF00875717

Saffer, D. M., & Marone, C. (2003). Comparison of smectite- and illite-rich gouge frictional properties: application to the updip limit of the seismogenic zone along subduction megathrusts. *Earth and Planetary Science Letters*, *215*(1–2), 219–235. https://doi.org/10.1016/S0012-821X(03)00424-2

Sánchez-Roa, C., Faulkner, D. R., Boulton, C., Jimenez-Millan, J., & Nieto, F. (2017). How phyllosilicate mineral structure affects fault strength in Mg-rich fault systems. *Geophysical Research Letters*, *44*, 5457–5467. https://doi.org/10.1002/2017GL073055

Schleicher, A. M., Boles, A., & van Der Pluijm, B. A. (2015). Response of natural smectite to seismogenic heating and potential implications for the 2011 Tohoku earthquake in the Japan Trench. *Geology*, *43*(9), 755–758.

Sawai, M., Hirose, T., & Kameda, J. (2014). Frictional properties of incoming pelagic sediments at the Japan Trench: implications for large slip at a shallow plate boundary during the 2011 Tohoku earthquake. *Earth, Planets and Space*, *66*(1), 1–8. https://doi.org/10.1186/1880-5981-66-65

Shimamoto, T., & Tsutsumi, A. (1994). A new rotary-shear high-speed frictional testing machine: its basic design and scope of research. *Journal of Tectonic Research Group Japan*, *39*, 65–78.

Sibson, R. H. (1975). Generation of Pseudotachylyte by Ancient Seismic Faulting. *Geophysical Journal International*, *43*(3), 775–794. https://doi.org/10.1111/j.1365-246X.1975.tb06195.x

Smeraglia, L., Bettucci, A., Billi, A., Carminati, E., Cavallo, A., Di Toro, G., et al. (2017). Microstructural evidence for seismic and aseismic slips along clay-bearing, carbonate faults. *Journal of Geophysical Research: Solid Earth*, *122*, 3895–3915. https://doi.org/10.1002/2017JB014042

Sone, H., Shimamoto, T., & Moore, D. E. (2012). Frictional properties of saponite-rich gouge from a serpentinite-bearing fault zone along the Gokasho-Arashima Tectonic Line, central Japan. *Journal of Structural Geology*, *38*, 172–182. https://doi.org/10.1016/j.jsg.2011.09.007

Tembe, S., Lockner, D. A., & Wong, T.-F. (2010). Effect of clay content and mineralogy on frictional sliding behavior of simulated gouges: Binary and ternary mixtures of quartz, illite, and montmorillonite. *Journal of Geophysical Research*, *115*, B03416. https://doi.org/10.1029/2009JB006383

Tesei, T., Lacroix, B., & Collettini, C. (2015). Fault strength in thin-skinned tectonic wedges across the smectite-illite transition: Constraints from friction experiments and critical tapers. *Geology*, *43*(10), 923–926. https://doi.org/10.1130/G36978.1

Turner, G. A. (1958). The flow-structure in packed beds: A theoretical investigation utilizing frequency response. *Chemical Engineering Science*, *7*(3), 156–165. https://doi.org/10.1016/0009-2509(58)80022-6

Ufer, K., Roth, G., Kleeberg, R., Stanjek, H., Dohrmann, R., & Bergmann, J. (2009). Description of X-ray powder pattern of turbostratically disordered layer structures with a Rietveld compatible approach. *Zeitschrift Für Kristallographie - Crystalline Materials*, *219*(9), 519–527. https://doi.org/10.1524/zkri.219.9.519.44039

Ujiie, K., Tanaka, H., Saito, T., Tsutsumi, A., Mori, J. J., Kameda, J., et al., & Expedition 343 and 343T Scientists (2013). Low Coseismic Shear Stress on the Tohoku-Oki Megathrust Determined from Laboratory Experiments. *Science*, *342*(6163), 1211–1214. https://doi.org/10.1126/science.1243485

Ujiie, K., Tsutsumi, A., & Kameda, J. (2011). Reproduction of thermal pressurization and fluidization of clay-rich fault gouges by high-velocity friction experiments and implications for seismic slip in natural faults. *Geological Society, London, Special Publications*, *359*(1), 267–285. https://doi.org/10.1144/SP359.15

Van Groos, A. K., & Guggenheim, S. Univ of I.(1987). Dehydration of a Ca- and a Mg-exchanged montmorillonite (SWy-1) at elevated pressures. *American Mineralogist; (USA)*, *72*, 3–4. Retrieved from. https://www.osti.gov/biblio/5152931

Van Groos, A. K., & Guggenheim, S. (1989). Dehydroxylation of Ca-and Mg-exchanged montmorillonite. *American Mineralogist*, *74*(5–6), 627–636.

Vannucchi, P., Spagnuolo, E., Aretusini, S., Di Toro, G., Ujiie, K., Tsutsumi, A., & Nielsen, S. (2017). Past seismic slip-to-the-trench recorded in Central America megathrust. *Nature Geoscience*, *10*(12), 935–940. https://doi.org/10.1038/s41561-017-0013-4

Vdović, N., Jurina, I., Škapin, S. D., & Sondi, I. (2010). The surface properties of clay minerals modified by intensive dry milling — revisited. *Applied Clay Science*, *48*(4), 575–580. https://doi.org/10.1016/j.clay.2010.03.006

Veveakis, E., Vardoulakis, I., & Toro, G. D. (2007). Thermoporomechanics of creeping landslides: The 1963 Vaiont slide, northern Italy. *Journal of Geophysical Research*, *112*, F03026. https://doi.org/10.1029/2006JF000702

Violay, M., Di Toro, G., Nielsen, S., Spagnuolo, E., & Burg, J. P. (2015). Thermo-mechanical pressurization of experimental faults in cohesive rocks during seismic slip. *Earth and Planetary Science Letters*, *429*, 1–10. https://doi.org/10.1016/j.epsl.2015.07.054

Vrolijk, P. (1990). On the mechanical role of smectite in subduction zones. *Geology*, *18*(8), 703–707. https://doi.org/10.1130/0091-7613(1990)018<0703:OTMROS>2.3.CO;2

Westphal, T., Füllmann, T., & Pöllmann, H. (2009). Rietveld quantification of amorphous portions with an internal standard—Mathematical consequences of the experimental approach. *Powder Diffraction*, *24*(03), 239–243. https://doi.org/10.1154/1.3187828

Wibberley, C. A. J., & Shimamoto, T. (2005). Earthquake slip weakening and asperities explained by thermal pressurization. *Nature*, *436*(7051), 689–692. https://doi.org/10.1038/nature03901

Wojatschke, J., Scuderi, M. M., Warr, L. N., Carpenter, B. M., Saffer, D. M., & Marone, C. (2016). Experimental constraints on the relationship between clay abundance, clay fabric, and frictional behavior for the Central Deforming Zone of the San Andreas Fault: CLAY FABRIC AND FRICTION. *Geochemistry, Geophysics, Geosystems*, *17*, 3865–3881. https://doi.org/10.1002/2016GC006500

Wu, F. T., Blatter, L., & Roberson, H. (1975). Clay gouges in the San Andreas fault system and their possible implications. *Pure and Applied Geophysics*, *113*(1), 87–95. https://doi.org/10.1007/BF01592901

Yamaguchi, A., Sakaguchi, A., Sakamoto, T., Iijima, K., Kameda, J., Kimura, G., et al. (2011). Progressive illitization in fault gouge caused by seismic slip propagation along a megasplay fault in the Nankai Trough. *Geology*, *39*(11), 995–998. https://doi.org/10.1130/G32038.1

Younglove, B. A., & Hanley, H. J. M. (1986). The Viscosity and Thermal Conductivity Coefficients of Gaseous and Liquid Argon. *Journal of Physical and Chemical Reference Data*, *15*(4), 1323–1337. https://doi.org/10.1063/1.555765

Yao, L., Ma, S., Niemeijer, A. R., Shimamoto, T., & Platt, J. D. (2016). Is frictional heating needed to cause dramatic weakening of nanoparticle gouge during seismic slip? Insights from friction experiments with variable thermal evolutions. *Geophysical Research Letters*, *43*, 6852–6860.